EVOLUTION OF CR-MO-V WELD METAL MICROSTRUCTURE DURING CREEP TESTING – PART 1: P91 MATERIAL

S.T. Mandziej[a] **A. Výrostková[b]**

[a] Advanced Materials Analysis (The Netherlands)
[b] Institute of Materials Research of Slovak Academy of Sciences (Slovak Republic)

ABSTRACT

Weld metal samples, manufactured in the recently concluded EU project "SmartWeld", were subjected to various creep tests followed by thorough metallographic and micro-analytical investigations, in order to explain their properties and to predict their long-term behaviour. The microstructural study concentrated on evolution of microstructure and transformations of carbides, which were assisting nucleation of voids and cracks in the creep tests. Results of the conventional constant load short-term/creep rupture test were compared with results of the newly developed accelerated creep test carried out on Gleeble physical simulator. The microstructures generated in these tests were compared with the initial microstructures of the weld metals as well as with microstructures of exploited / crept materials. Most of the effort was dedicated to identification of precipitated phases, mainly carbides, as well as to their transformations. The metallographic study, mainly carried out by means of transmission electron microscopy on carbon extraction replicas and also by scanning electron microscopy on fractures with implementation of EDS x-ray microanalysis, was supplemented by Thermocalc calculations for the appearance of phases at equilibrium conditions. Then, using thin foil technique in TEM, the recovery and recrystallisation of the initial martensitic-bainitic microstructure of the weld metal matrix was studied and the formation of subgrains and grains observed. Finally, the changes in the substructure were correlated with nucleation of fractures / failure modes of various creep tests. In general, the acceleration of creep-like transformation of microstructure appeared dependent on accumulated or localised strain exerted by the testing method. Nevertheless, compatibility of the used tests was confirmed with indication of several nuances affecting variations of the final micro- and sub-structures of the investigated weld metals after exposure to the creep test conditions.

IIW-Thesaurus keywords: *Arc welding; Comparisons; Creep resisting materials; Creep tests; Heat treatment; Mechanical tests; Microstructure; MMA welding; Post weld heat treatment; Weld metal.*

1 INTRODUCTION

Design of the power plant components and inherent estimation of power plants lifetime is based on long-term creep data, which are generally available for the used plate and pipe creep resisting materials. However, for the welds on the components of the power plants, such data are not always easily found. This is mainly due to the large variety of factors appearing in the fabrication procedure, which affect the creep strength and creep life of the welds. To predict the exploitation behaviour of the welds under creep, especially the repair welds, accelerated creep testing (ACT) procedures can be used. Such procedures of accelerated tests, developed usually to predict the time to failure of critical power generation components, often apply small strains and/or constant slow deformation rates to accelerate microstructural transformation processes characteristic of metal alloys exploited at creep conditions [1]. In gen-

Doc. IIW-1822-07 (ex-doc. II-1601-06) recommended for publication by Commission II "Arc Welding and Filler Metals".

eral, they aim to determine in a relatively short time the creep strength or remaining ductility which the creep resisting materials would have after their long exposure to stresses at the elevated temperatures characteristic of their exploitation.

A new accelerated creep test has been recently developed by the Advanced Materials Analysis, Enschede, Netherlands, in collaboration with Dynamic Systems Inc, Poestenkill NY, USA [2]. This ACT procedure is a low-cycle thermal-mechanical fatigue test implemented on Gleeble physical simulator, based on the actual knowledge of the micro- and sub-structural changes causing decay of properties during creep. To simulate the situation of material deteriorating during creep, the following demands had to be achieved in the ACT:

– Total deformation at fracture being like at real creep – just a few percent only.

– Depletion of weld metal or steel matrix in alloying elements achieved similar to that of long-term crept steels and the carbide phases at onset of cracks must not be different.

– Basic temperature and applied strains in the ACT preventing odd transformations like secondary dissolution of carbides and/or formation of far from equilibrium phases.

These aims have been reached by considering that certain dislocations can effectively dissolve and then transport interstitial elements like C & N, and that the annihilation of these dislocations may control the precipitation of carbides [3]. Thus accumulation of strains, generating appropriate dislocation configurations and increasing level of stored energy in the steel, was used to speed-up the transformation of microstructure. An additional factor used in the development of ACT, known for a long time as capable of accelerating recrystallization of matrix and coagulation of carbides [4], was an electric resistance heating with controlled thermal gradients.

The above-mentioned initial ACT procedure [2] was implemented in the “SmartWeld” project and on purpose modified in the course of it [5]. What follows in this article is the presentation of selected ACT results and their comparison with the results of conventional creep-rupture tests as well as with data available for the materials crept in exploitation conditions. As the reliability of any elevated temperature test, and the ACT cannot be an exception, must be confirmed by the microstructure evolution i.e. the precipitation processes and sequence of changes leading to failure, that reproduce the situations occurring in real creep, the major part of this work is devoted to this. Presented here are data obtained for P91 type weld metals, although in the “SmartWeld” project other materials like P22, P23 and P24 were also studied. Results of studies on these last materials should be presented in subsequent reports later.

In the actually running COST 536 and COST 538 Actions of the European Science Foundation this ACT procedure is being applied to predicting remnant lifetime of partly exploited crept components as well as to evaluating in a very short time the anticipated long-term creep properties of newly developed materials. The up-to-date ACT procedure is there considered as having a capability of ranking the creep resisting materials for their expected creep behaviour.

2 THE SIMULATIVE ACCELERATED CREEP TEST ON GLEEBLE – ACT

To carry out the simulative accelerated creep tests, new Gleeble 3500 physical simulator was used. In such simulator the balance between electric resistance heating of the sample and the heat flow by thermal conductivity of this sample towards the cold copper mounting jaws allows forming a uniformly heated zone in the middle-span of the sample (like shown in Figure 1). To better define this zone, a gauge portion of reduced diameter was made on the sample.

In this study samples of new P91 weld metals were tested, taken across multi-bead, multi-layer welded joints, as shown in Figure 2, allowing testing either all-weld

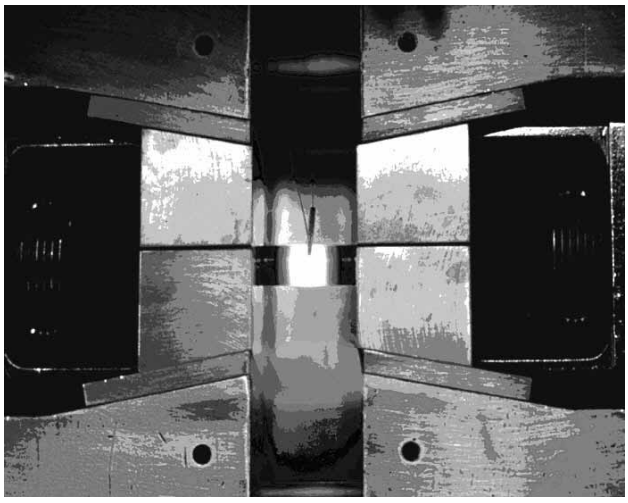

Figure 1 – Example of uniformly heated zone formed in Gleeble at the mid-span of the rod-like specimen (at temperature much higher than used in the ACT)

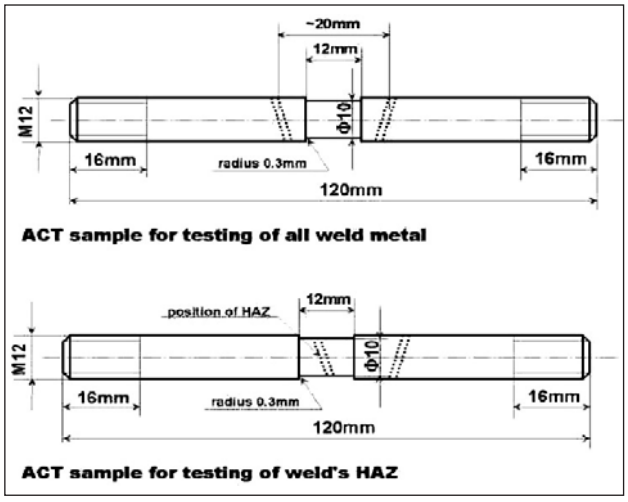

Figure 2 – Cross-weld samples used for ACT on all-weld metal and on weld’s HAZ in the “SmartWeld“ EU projec

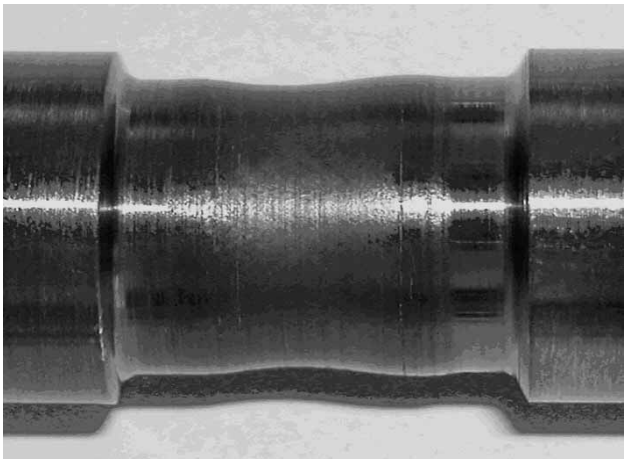

Figure 3 – Mid-portion of the all-weld metal, sample after the ACT, run till drop of the initial material strength to one-third

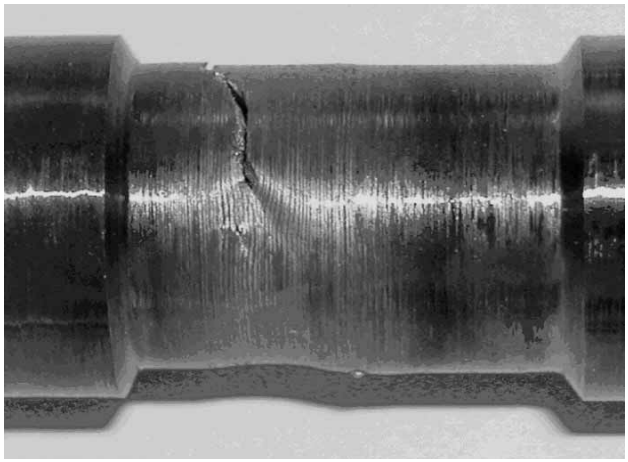

Figure 4 – Mid-portion of the weldment HAZ sample after the ACT, run till initiation of the crack along the HAZ

metal or the heat-affected zone of the weld. The following Figure 3 shows central portion of the all-weld metal sample after the ACT run to a programmed minimum relaxation force (i.e. before full cracking), while Figure 4 shows the initiation of cracking in HAZ sample.

Using various consumables, the all-weld metal P91 samples were prepared by FCW process (material 1m/2m) and by MMA process (materials 5m/6m, 5s/8s and 10s). Odd numbered samples were examined in as-welded state, while the even numbered were examined after PWHT.

The chemical compositions of the manufactured weld metals are given in Table 1.

Based on results of initial mechanical testing and metallographic examination, these materials could be characterized as:

– 1m & 2m; medium-high hot strength / low temperability material of initial auto-tempered martensite microstructure;

– 5m & 6m; high hot strength / high temperability material of initial soft martensitic / ferritic microstructure;

– 5s & 8s; medium strength material of initial bainitic / martensitic microstructure, components of which do not temper at the same time;

– 10s; an optimised high strength material of bainitic / martensitic microstructure, in which the precipitation processes and sequence of matrix transformations should offer an extended creep life.

In each thermal-mechanical cycle of the ACT the quasi-static (strain rate of ~ 0.001/sec) tensile elasticity modulus at the elevated temperature of the test could be measured and its decrease with the duration of the test could be observed. So was observed the decrease of tensile yield strength during relaxation time on the ACT samples under tension.

Most of the ACT samples were tested till fracture occurred, however some of them especially these for fine fractographic observations and microanalytical investigations were stopped before fracturing. As the tests for different materials were run at different temperatures, as well as the need occurred to compare the ACT results obtained at various temperatures, the duration of the test and its temperature have been included in the following parameter:

$$PACT = (7 + \log t) * T/100$$

where:
t = time of test in [ksec], and
T = temperature in [K].

Table 1 – Chemical composition of P91 weld metals

Material	Element [wt.%]						
	C	Mn	Si	Cr	Ni	Mo	Nb
1m & 2m	0.11	0.94	0.32	9.43	0.50	1.05	0.036
5m & 6m	0.089	0.54	0.26	8.58	0.34	0.97	0.044
5s & 8s	0.06	0.59	0.36	9.49	0.94	0.98	0.005
10 s	0.09	0.84	0.40	8.70	0.40	0.93	0.061

Material	Element [wt.%]						
	B	V	Ti	W	N	Cu	Al
1m & 2m		0.22	0.060		0.043	0.03	0.010
5m & 6m		0.19	0.005		0.036	0.02	0.009
5s & 8s	0.0005	0.21		0.21	0.012		0.001
10s	0.0005	0.20	0.008	0.01	0.052		0.003

Then, the creep strength factor in ACT has been calculated as

FACT = PACT * RS /100

where

R_S is the average stress of all ACT cycles measured during relaxation on tension.

Selected examples strain-time and stress-time graphs from ACT are given in Figures 5 to 10. For “soft”, e.g. over-tempered materials, the zero-stress line on the strain-time curve well resembles a normal creep graph with its three characteristic stages, see Figure 5. For the materials after optimised treatment, e.g. after a temper-bead welding or proper PWHT, somewhat different strain-time behaviour was observed in ACT, with a long period of monotonously increasing length of the sample, Figure 7, while for “hard” materials like some as-welded joints without any PWHT often a straight continuous

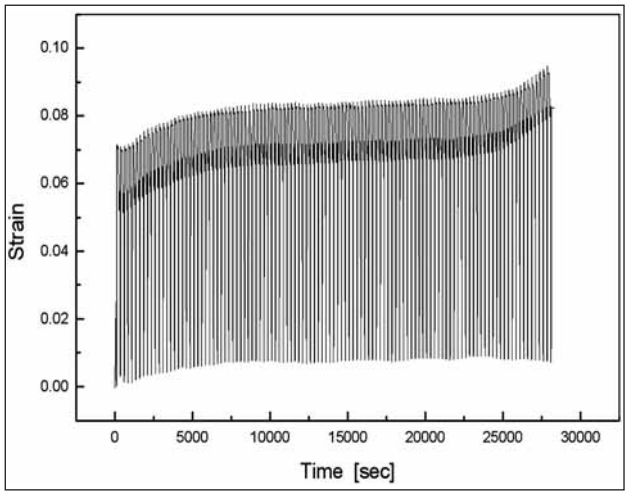

Figure 5 – Typical strain-time graph from ACT on a “soft” weld metal

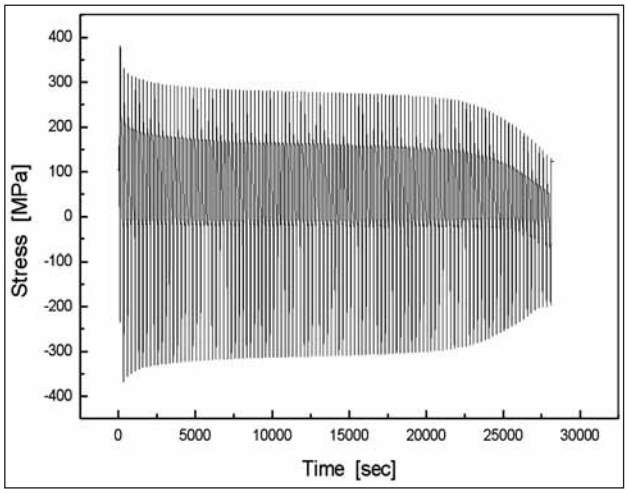

Figure 6 – Typical stress-time graph from ACT on a “soft” weld metal

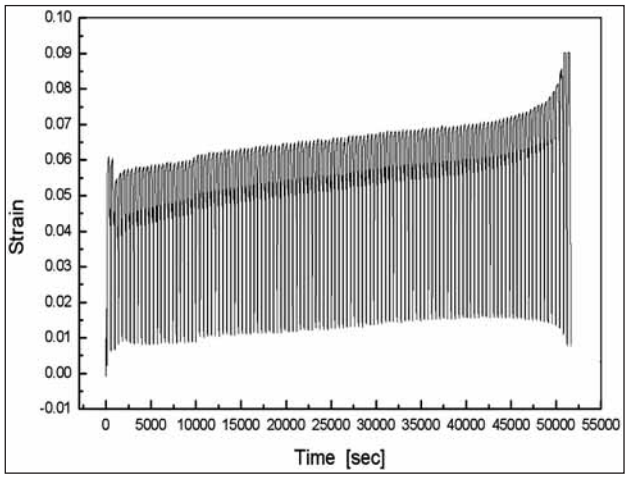

Figure 7 – Typical strain-time graph from ACT on an optimally processed weld metal

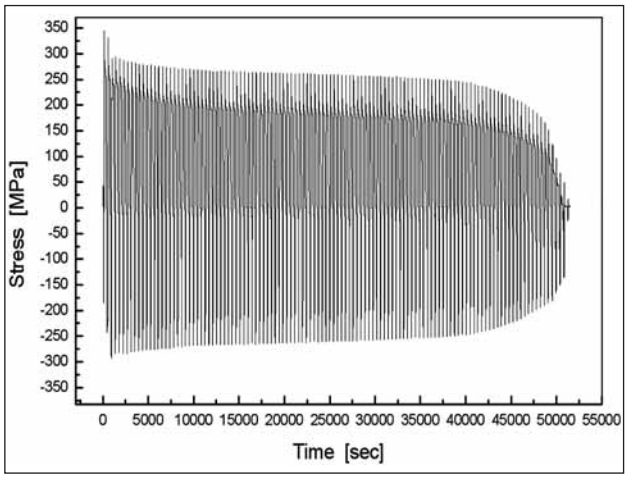

Figure 8 – Typical stress-time graph from ACT on an optimally processed weld metal

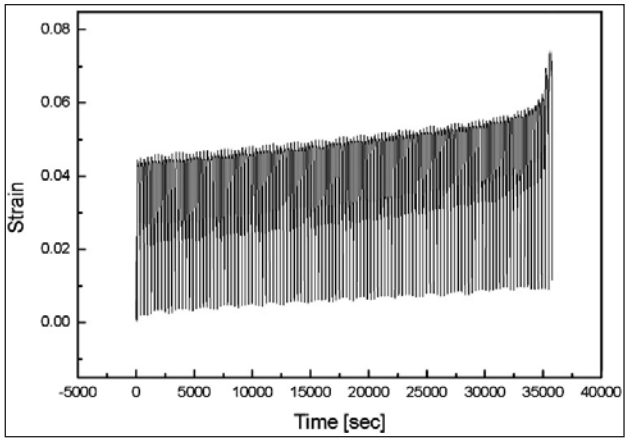

Figure 9 – Typical strain-time graph from ACT on a “hard” weld metal

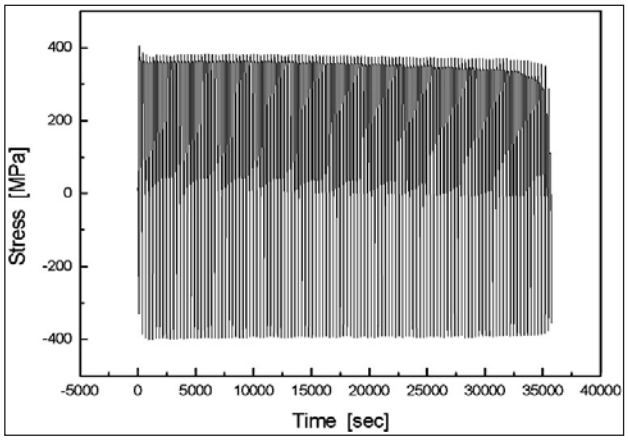

Figure 10 – Typical stress-time graph from ACT on a “hard” weld metal

elongation in each cycle was observed from beginning till the end of test, Figure 9. In this last case, the elevated temperature yield strength of material decreased very little during the test, Figure 10, and its final fracture was often semi-brittle / quasi-intergranular.

A bit more about the material behaviour can be learned while analyzing individual thermal-mechanical cycles of the ACT procedure. Thus for non creep resistant materials as well as for most of the tested materials by the end of the creep test (ACT) characteristic behaviour during relaxation under tensile stress comprises plastic elongation of sample during which the stress drops; this can be seen in Figures 11 and 12.

However when the material subjected to ACT is still "creep-strong", a variety of microstructural / substructural processes appear during the relaxation, in particular generation and annihilation of dislocations, rearrangement of grain boundaries, strain-induced precipitation and coagulation of carbides. In result, often instead of weakening and extending the ACT sample can even shrink and strengthen during the tensile relaxation period. An example of such irregularity is given in Figures 13 and 14.

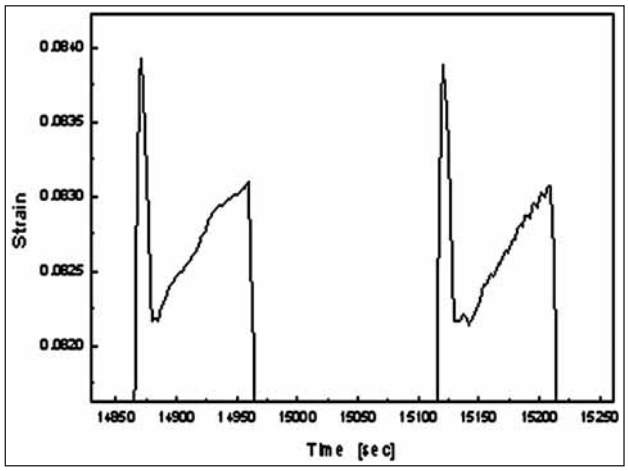

Figure 11 – Permanent extensions during tensile relaxation in individual cycles of the ACT on a weak creep resistant sample

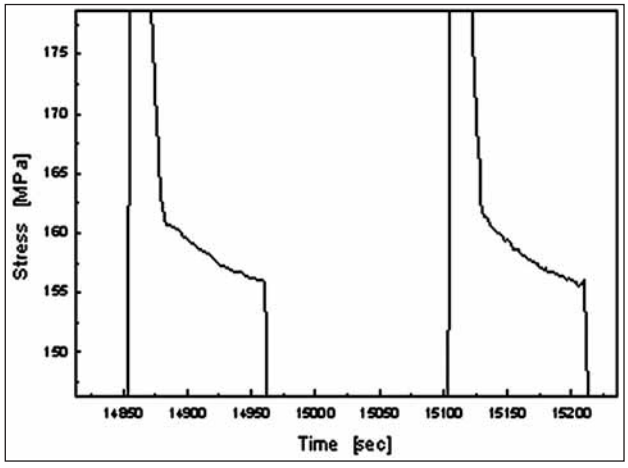

Figure 12 – Typical stress drop during tensile relaxation in individual cycles of the ACT on a weak creep resistant sample

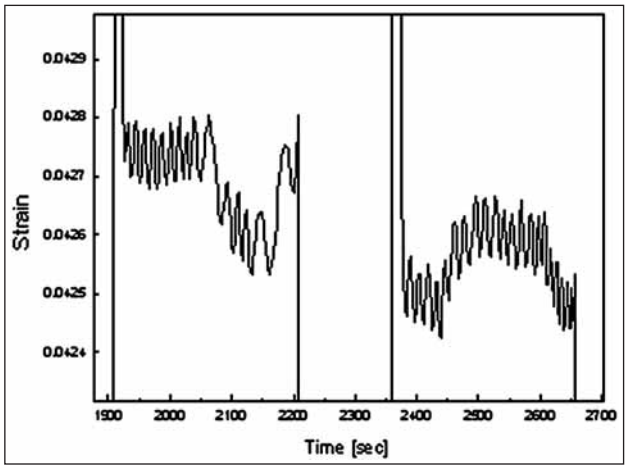

Figure 13 – Irregular extensions and shrinkages during tensile relaxation in individual cycles of the ACT on a strong creep resistant sample

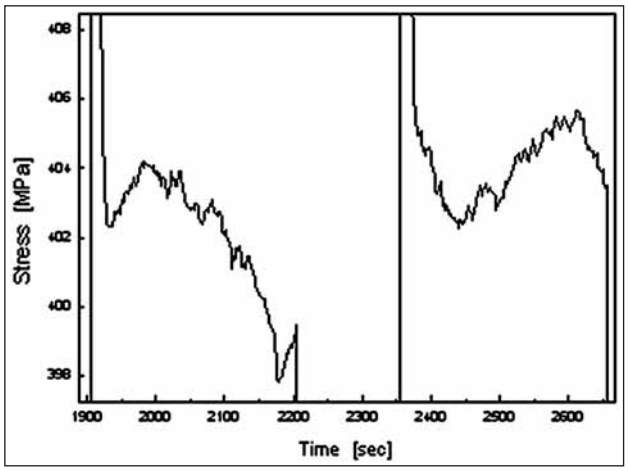

Figure 14 – Build-ups and drops of stress during tensile relaxation in individual cycles of the ACT on a strong creep resistant sample

Selected examples of the ACT results on P91 weld metals are given in Table 2. They show in general higher creep strength of non heat-treated weld metals, tendency of increasing time to fracture by PWHT due to changing of failure micromechanism (compare 1m with 2m and 5m with 6m). They also show positive compromise results of optimizing heat treatment (5s vs. 8s) as well as chemical composition together with heat treatment (10s).

As in parallel short-term creep-rupture tests (STCT) were run on most of these materials, the results of both tests could be compared. Selected results of the STCT are given in Table 3 and compared with these of the ACT. The creep strength factor – F_{CS} – given in this table was calculated from the STCT results like:

FCS = PLM * RL/100

where

R_L is the initial stress of the constant-load short-term creep experiment, and

P_{LM} is the Larson-Miller parameter:
$P_{LM} = (20 + \log t) * T/100$,

with
T = testing temp. in [K], and
t = time to rupture in [h].

Table 2 – Examples of ACT results

Sample number	Maker / source	Material & state	ACT temp. [deg C]	ACT time to fracture [ksec]	Tensile relax stress R_S [MPa]	Creep strength factor F_{ACT} [MPa]
1m	MPL	P91-AW	625	22.0	305	228
2m	MPL	P91-HT	625	37.6	273	210
5m	MPL	P91-AW	620	38.0	395	303
6m	MPL	P91-HT	620	51.3	177	138
5s	SSW	P91-HT	600	28.3	325	240
8s	SSW	P91-HT	600	26.3	318	233
10s	SSW	P91-HT	600	82.6	336	262

Table 3 – Comparison of results: ACT vs. STCT

Sample No.	Material & state	STCT results: [temp./stress/time]	F_{CS} [MPa]	F_{ACT} [MPa]	F_{CS} / F_{ACT}
1m	P91-AW	650/150/416	355	228	1.56
2m	P91-HT	650/150/30	293	210	1.39
5m	P91-AW	620/150/1995	312	303	1.03
6m	P91-HT	620/130/282	261	138	1.89
5s	P91-AW	620/130/381	262	240	1.09
8s	P91-HT	620/130/31	249	233	1.07

It may be noted here that for the strong or optimally treated materials the correlation of F_{CS} / F_{ACT} is near to 1.0 while for weaker, e.g. highly tempered materials, it reaches values from 1.5 to 2.0.

3 STUDY ON REFERENCE MATERIALS

For this study STCT samples of P91 steel and a crept P91 component consisting of antler / stub / weld, were made available from E.ON (PTC), UK. Also the P91 material in initial state, of the same batch that was used for the STCT (KA817), was provided. The chemical compositions of these materials are given in Table 4.

The chemical composition of the weld between the stub and the antler in the sample of the crept component was matching this of the antler. The sample of this crept component was taken from the location near to found intensive creep damage and could be considered as being close to the end of life in creep.

These reference materials were subjected to metallographic investigations in order to determine the advancement of microstructure evolution due to creep. At first the microstructure of the KA817 materials was examined in as-delivered state, i.e. before exposure to creep. Then micro-structural investigation was carried out on samples of this material after short-term creep tests and finally samples of this batch after ACT were examined. Also the microstructure observations and phase identification was carried out on the antler/weld/ stub sample. This part of the work was mainly done by transmission electron microscopy using for the identification and characterization of phases selected-area electron diffraction and EDS microanalysis on carbon extraction replicas and to a less extent observations on thin foil specimens. Thermocalc calculations of phase equilibria were done as well. The results are summarised in Table 5.

The samples of P91 steel / KA817 batch in the as-delivered state and after STCT have been used as the first reference material for the further microstructural evaluation in this study. The study revealed, in general, various post-martensitic structures in which the principal carbides phases remained the same (dominating $M_{23}C_6$ carbide) and the major differences were in the sizes and distribution of the carbides.

In the as-delivered state, i.e. heat treated after hot rolling, the P91 steel / batch KA817 has a microstructure of tempered martensite with partly coagulated carbides;

Table 4 – Chemical compositions of reference P91 materials

Sample	Element (wt.%)									
	C	Mn	Si	Cr	Ni	Mo	V	Ti	Nb	N
KA 817	0.13	0.48	0.28	8.59		0.97	0.21	0.003	0.081	0.056
KA 1344/3/ stub	0.09	0.39	0.44	8.73	0.12	0.84	0.19		0.090	0.050
KA 1344/3/ antler	0.10	0.42	0.28	8.01	0.14	0.92	0.21		0.060	0.045

Table 5 – Phase compositions of reference materials

Sample	Creep (test) conditions	Phase composition / carbides						
		M_3C	$M_{23}C_6$	M_7C_3	M_2X	M_6C	MX	Laves
KA817/1/8	As received		x		x		x	
KA817/1/5 # 1992	STCT – 600 °C/155 MPa/1 416 h		x				x	L
KA817/1/5 # 1993	STCT – 650 °C/104 MPa/969 h		x				x	
KA817/1/5 # 1994	STCT – 690 °C/65 MPa/1 384 h		x				x	(L)
KA817 – K2	ACT – 625 °C/28.3 ksec		x				x	
KA817	Thermocalc phase content at 600 °C		X				X	L
KA817	Thermocalc phase content at 650-690 °C		X				X	
KA1344/3 antler	Exploited ~ 600 °C/170 bar/9 years		x				x	L
KA1344/3 stub	Exploited ~ 600 °C/170 bar/9 years		x				x	L
KA1344/3 weld	Exploited ~ 600 °C/170 bar/9 years		x				x	L
KA1344/3 antler	Thermocalc phase content at 550-640 °C		X				X	L
KA1344/3 stub	Thermocalc phase content at 550-640 °C		X				X	L

the dominating medium size carbides were of $M_{23}C_6$ type while fine dispersed carbides were MX type, Figure 15.

After the short-term / creep rupture tests, carbide coagulation and recrystallisation of matrix were progressing with increase of temperature. Accordingly, the STCT sample # 1992, tested at 600 °C, contains substantial amount of subgrains in arrays of the post-martensitic orientations, Figures 16 & 17, while after testing at

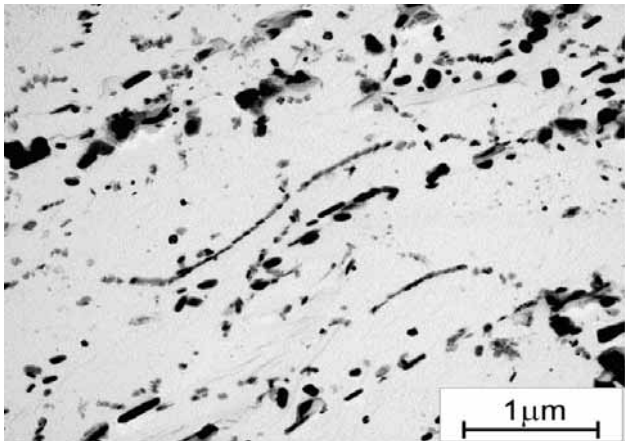

Figure 15 – Image of carbon extraction replica taken from P91 material batch KA817 in as-delivered state (hot rolled & tempered); small and medium size carbides in arrays retaining former orientations of martensite laths

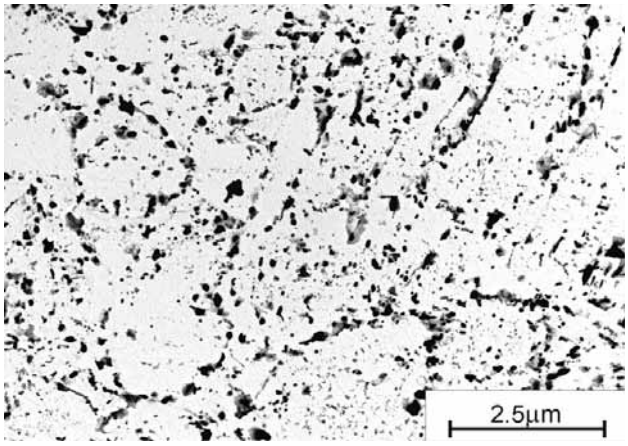

Figure 16 – Image of carbon extraction replica taken from P91 material batch KA817 after STCT at 600 °C (sample # 1992); chains of coagulated carbides deposited along boundaries of former martensite laths and of recrystallised ferrite grains

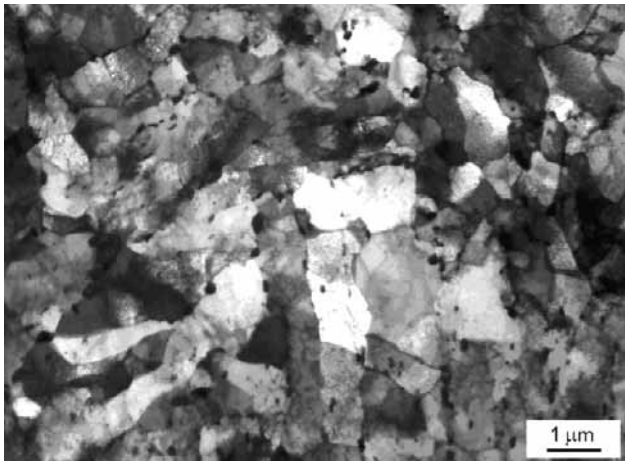

Figure 17 – Fine equiaxial ferrite subgrains as well as post-martensitic elongated subgrains in P91/KA817 sample # 1992 after STCT at 600 °C

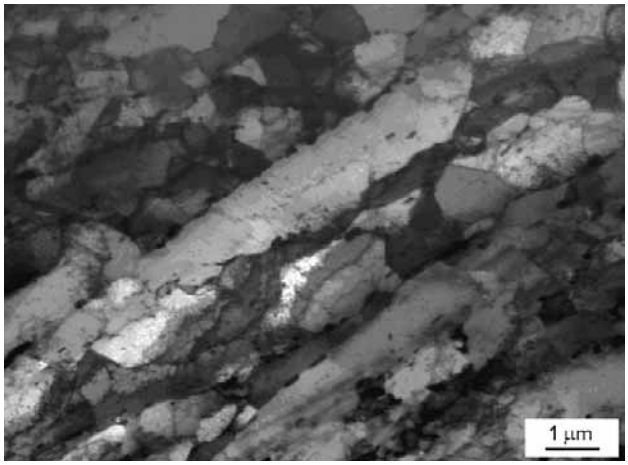

Figure 18 – Elongated ferrite subgrains, following orientations of former martensite laths in P91/KA817 sample # 1992 after STCT at 600 °C

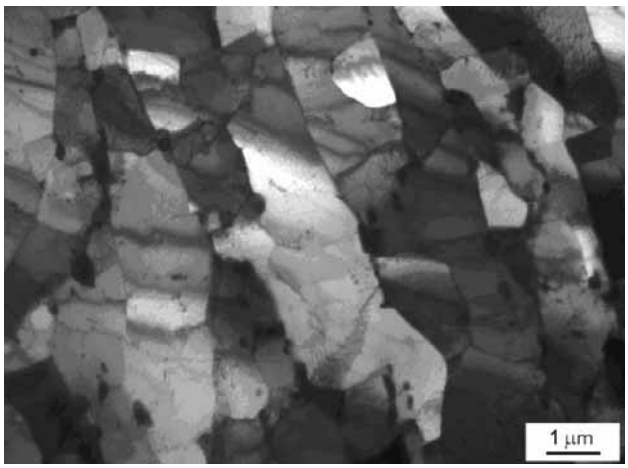

Figure 19 – Lateral growth, as compared with sample # 1992, of post-martensitic elongated ferrite subgrains, observed in P91/KA817 sample # 1993 after STCT at 650 °C

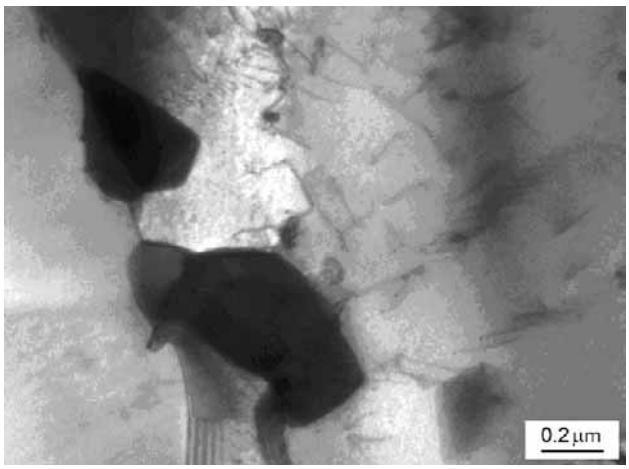

Figure 20 – Large coagulated carbides at boundaries of recrystallised ferrite grains in P91/KA817 sample # 1994 after STCT at 690 °C

650 °C (sample # 1993) this effect diminishes, Figure 18. Finally, after STCT at 690 °C (sample # 1994) the matrix consists of recrystallised ferrite grains with coagulated carbides, Figures 19 & 20.

The as-delivered P91/KA817 material was also subjected to the accelerated creep testing on Gleeble. After ACT at 625 °C the microstructure of P91 steel batch KA817 (Figure 21) did change as compared with the initial state (see Figure 15); the carbides became larger and more coagulated, while being distributed mainly along grain boundaries of recrystallised ferrite grains and their amount inside grains decreased. This microstructure quite well resembles that of STCT at 650 °C (sample # 1993), Figure 22, as to the sizes of ferrite grains / subgrains and of carbides and is certainly more transformed than after STCT at 600 °C (sample # 1992, Figure 16).

Characteristic of the P91/KA817 material after the ACT was a relatively high dislocation density in some ferrite grains, observed in particular in these samples, testing of which was stopped before the full fracture occurred. In microstructure after the ACT the majority of carbides appeared along boundaries of recrystallised ferrite grains, Figure 23. At “triple points” between the grains larger colonies of carbides were formed and high dislocation density was retained, Figure 24. Most of the $M_{23}C_6$ carbides did spheroidise, Figure 25, and a suggestion might be made that some dislocations cutting through carbides inside ferrite grains did participate in the accelerated dissolution of these carbides, Figure 26.

As the second reference material for comparison of microstructures with these generated by ACT, a sample of a crept P91 component has been taken into consideration. It was a piece of a power-generating installation, which had been operating at creep conditions for 9 years at the temperature of ~ 600 °C and at a pressure of about 170 bar. The examined piece of tube, of nominally 57 mm outer diameter x 6.3 mm wall thickness, comprised portions of stub and antler with a weld between them. Related chemical compositions of stub and antler are given in Table 4. The weld metal composition was selected to match the chemical compositions of the antler component. In the exploited state, the hardness was of about 150 HV for antler (A) and 175 HV for stub (S), indicating close to the end-of-life condition.

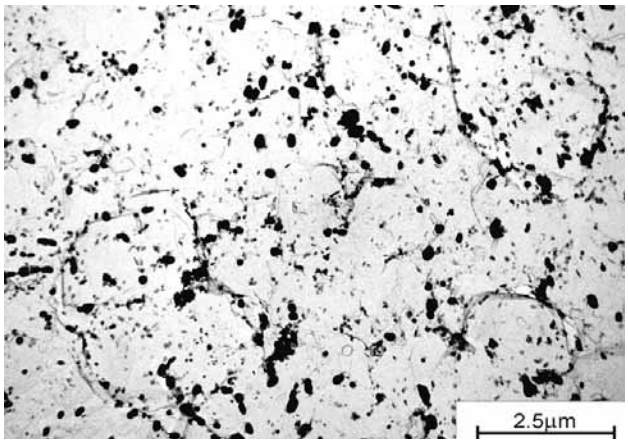

Figure 21 – Microstructure of P91/KA817 steel after ACT at 625 °C; numerous coagulated carbides distributed along grain boundaries of recrystallised ferrite

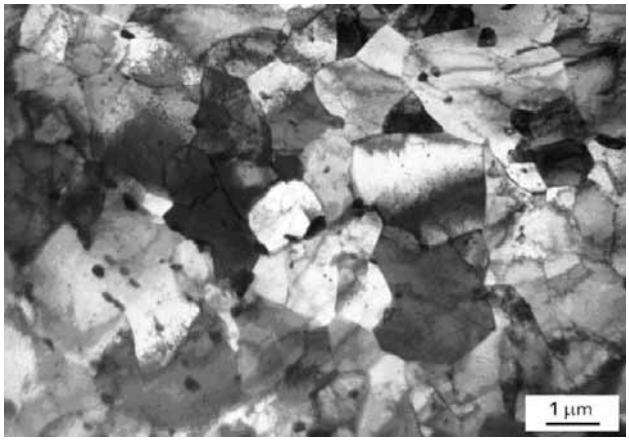

Figure 22 – Microstructure of P91/KA817 steel after STCT at 650 °C (sample # 1993); similar size of ferrite grains / subgrains and carbides like in Figure 21

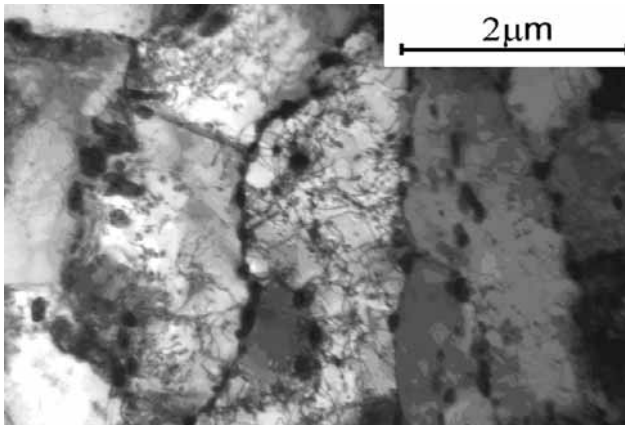

Figure 23 – Microstructure after the ACT showing majority of carbides appearing along boundaries of recrystallised ferrite grains

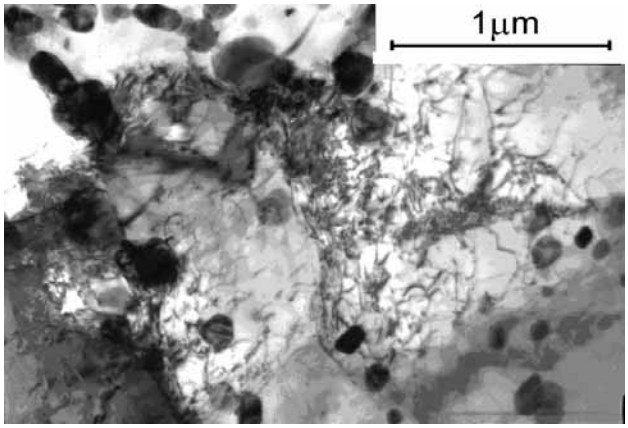

Figure 24 – A colony of larger than average carbides and high dislocation density at a "triple point" between the ferrite grains

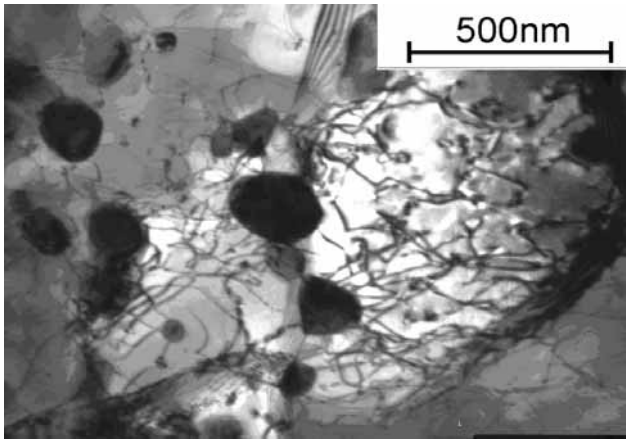

Figure 25 – Spheroidised $M_{23}C_6$ carbides in recrystallised ferrite after the ACT

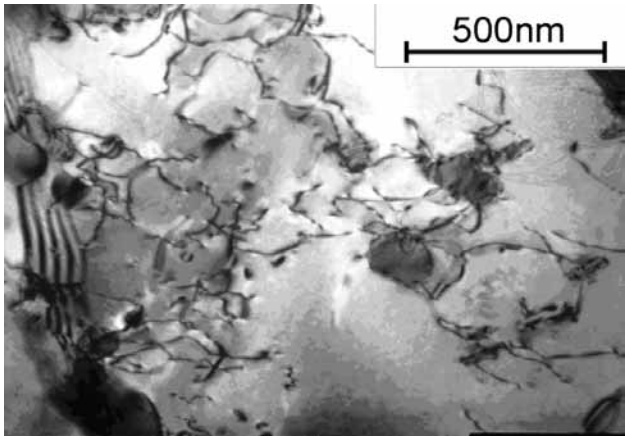

Figure 26 – Dislocations cutting through carbides inside recrystallised ferrite grains

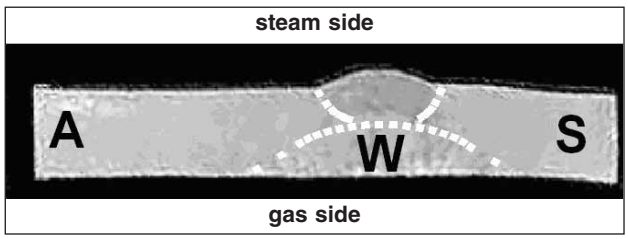

A – Antler *W – Weld* ***S – Stub***

Figure 27 – Macro-photograph of the sample taken from a crept component of power-generating installation

Figure 27 shows the situation of both elements and the weld between them; an enlarged fragment of this is presented in Figure 28, with darker etched areas in the stub piece beyond the HAZ of the weld. After further examination by SEM, these dark spots appeared not to be any voids only etching effects, while a number of creep voids were found along prior austenite grain boundaries in the transformed P91 microstructure of the antler, Figure 29.

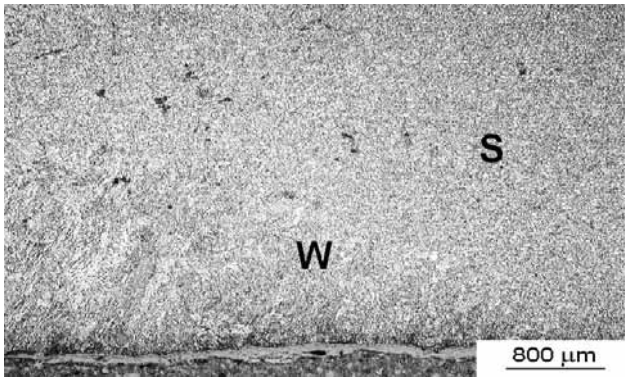

Figure 28 – A low-magnification micrograph of stub and weld portions of the sample

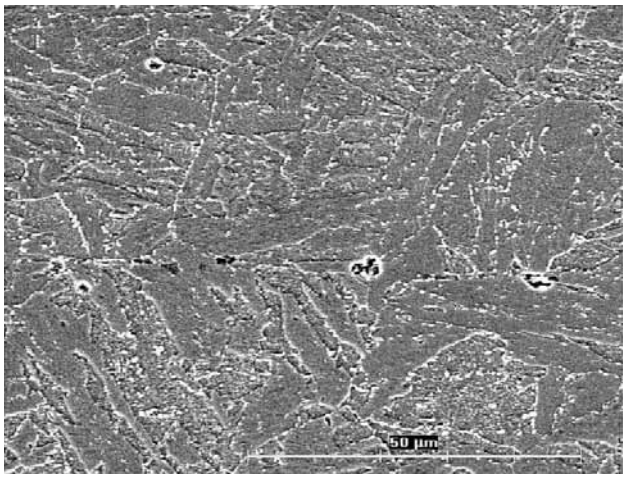

Figure 29 – Creep voids along prior austenite grain boundaries in the antler

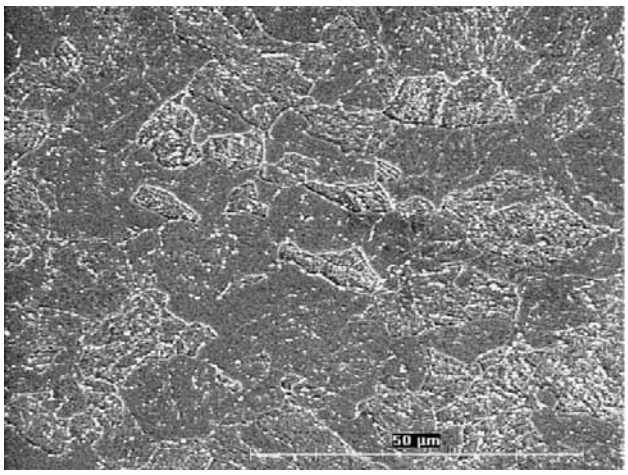

Figure 30 – Finer grains of prior austenite in the stub, with no creep voids

No voids could be found in the stub material, having the finer prior austenite grains, Figure 30.

In the weld some voids were found in its outer portion / on gas side of the pipe, Figure 31, while no voids could be observed in the inner weld bead / from the steam side. The inner weld bead appeared more recrystallised, containing larger coagulated precipitates, Figure 32, while the outer / gas side weld bead retained its columnar structure with dense precipitation at roots of columnar grains; in these sites also the creep voids appeared.

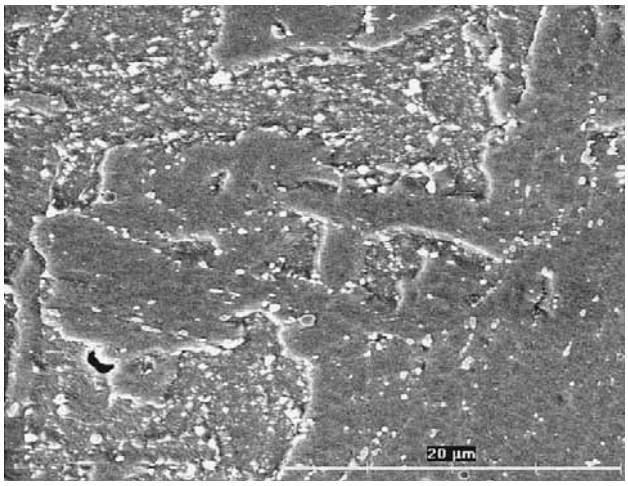

Figure 31 – Creep voids in the transformed microstructure of the gas-side weld bead

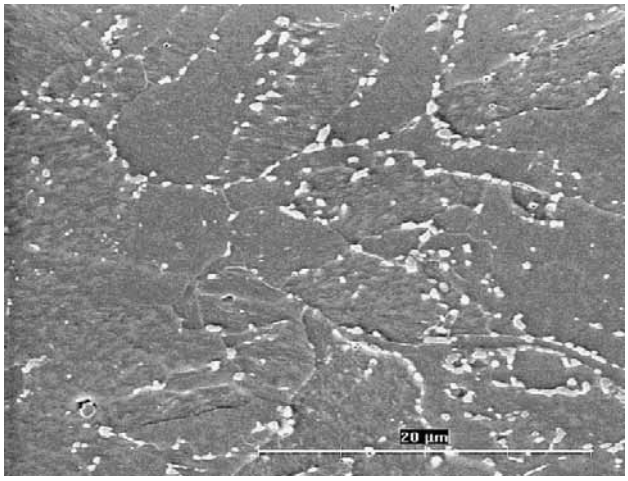

Figure 32 – No creep voids in the steam-side weld bead

Similar advancement of the microstructure transformation of the weld was observed by light microscopy, as shown in Figures 33 and 34 (outer & inner bead, respectively). At larger magnification of the light microscope the precipitates in the gas side weld bead appeared to be spheroidal, aligned in chains keeping orientation of the former martensite laths, Figure 35.

TEM observations on thin foils showed advanced recrystallisation of ferrite matrix, while the chains of precipitates

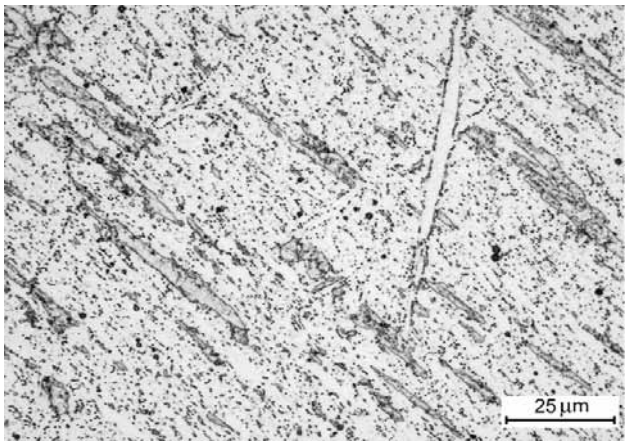

Figure 33 – Microstructure of transformed columnar grains in the outer weld bead

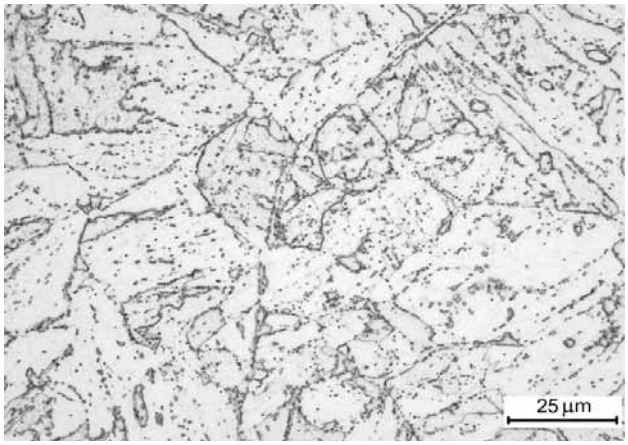

Figure 34 – Microstructure of transformed martensite of the inner weld bead

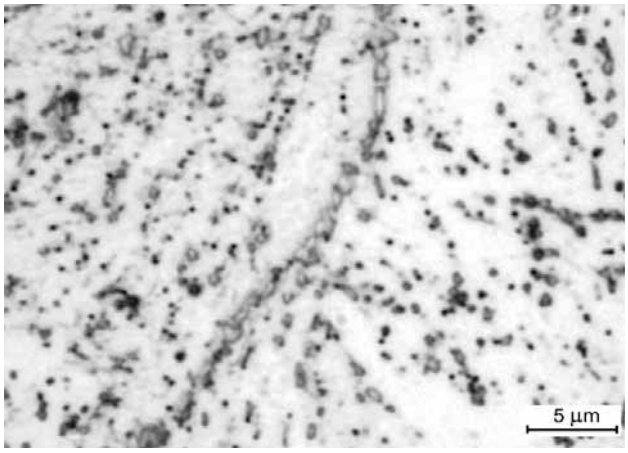

Figure 35 – Spheroidal carbides in the outer weld bead, on the gas-side of the sample

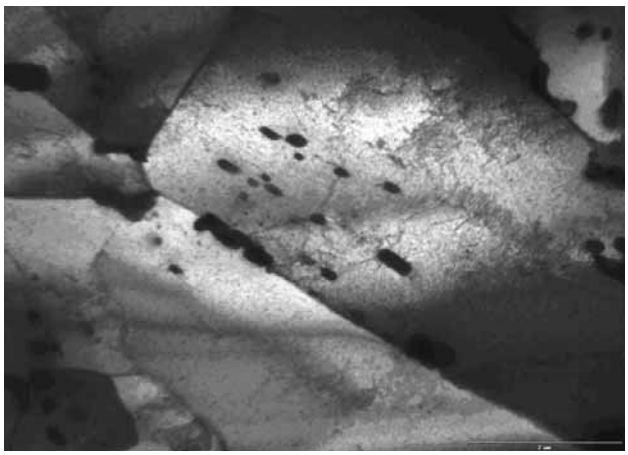

Figure 36 – Recrystallised ferrite grains of the weld metal in the inner bead of the weld

retained their prior orientation within the recrystallised grains, Figure 36.

The crept "parent" materials, i.e. of the antler and stub, appeared in light microscopy as consisting of only equiaxial entirely recrystallised grains with a large number of uniformly distributed spheroidal precipitates, Figures 37 and 38. Visibly larger, i.e. more coagulated carbides could be distinguished in the stub material (Figure 38).

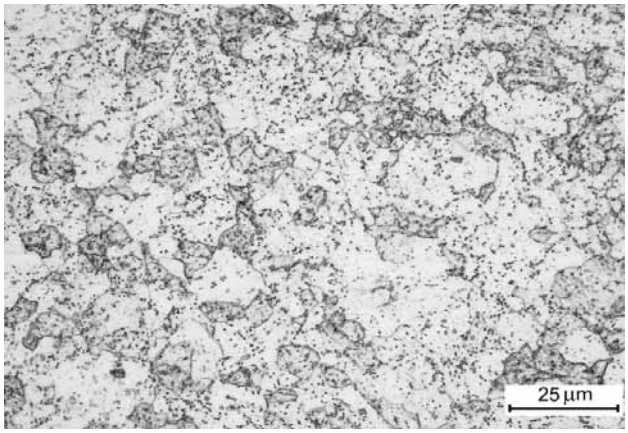

Figure 37 – Microstructure of the ~ 600 °C/ 170 bar/9 years crept P91 antler; uniformly distributed carbides in recrystallised ferrite matrix

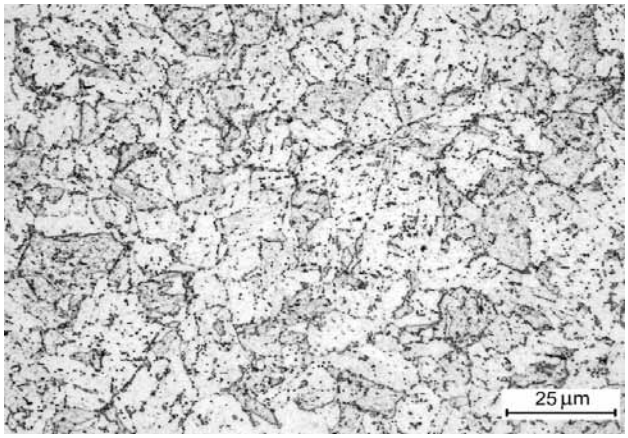

Figure 38 – Microstructure of the ~ 600 °C/ 170 bar/9 years crept P91 stub; uniformly distributed carbides in recrystallised ferrite matrix

Transmission electron microscope observations on thin foil specimens taken from the stub and antler materials revealed in general the advanced recrystallisation in both of them, although in the antler material numerous regions of subgrains of post-martensitic orientation were observed, Figure 39, and the grains of ferrite matrix, recrystallised by coalescence of such subgrains, often retained this orientation of the former martensite, Figure 40.

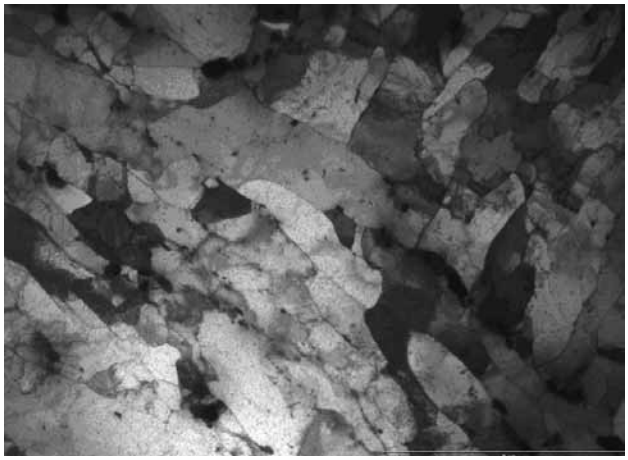

Figure 39 – Microstructure of the ~ 600 °C/ 170 bar/9 years crept P91 antler; bundles of post-martensitic subgrains between larger grains of recrystallised ferrite

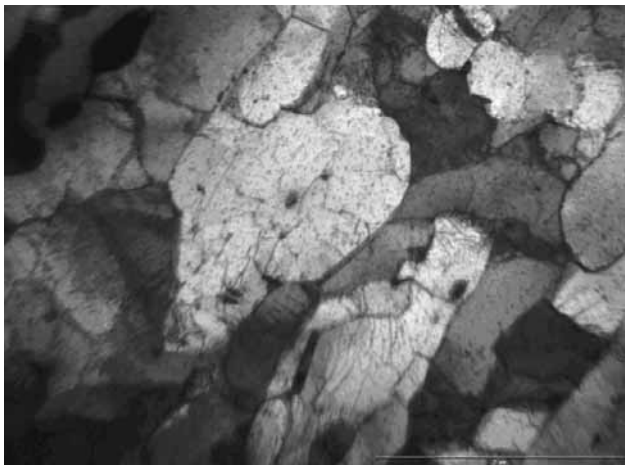

Figure 40 – Microstructure of the ~ 600 °C/ 170 bar/9 years crept P91 antler; recrystallised ferrite grains growing by coalescence of subgrains

4 PHASE EVOLUTION IN P91 WELD METALS DURING CREEP TESTING

The phase compositions of the investigated P91 weld metals were determined by transmission electron microscopy with the use of EDS x-ray microanalysis and electron diffraction. Most of the identification was done on carbon extraction replicas, while the replicas were taken from cross-sections of the samples as well as from fractures. Some additional results were obtained from thin foil specimens examined in TEM. The summary of the phase identification is given in Table 6.

Table 6 – Phase compositions of selected P91 weld metals (from carbon extraction replicas/EDS)

Sample & treatment	Accelerated creep test conditions	Phase composition / carbides						
		M_3C	$M_{23}C_6$	M_7C_3	M_2X	M_6C	MX	Laves etc
1m – AW	Initial state		x	x			(x)	Z
FCW, P91	STCT – 650 °C /150/416 h			x			x	
	ACT – 625 °C/22.0 ksec		x		x		(x)	
	ACT – 625 °C/22.0 ksec (fr)		x			x	(x)	L
2m – HT	Initial state		x	x	x	x	x	
FCW, P91	STCT – 650 °C /150/30 h		x	x		x	x	
	ACT – 625 °C/37.6 ksec		x				x	
1m & 2m	Thermocalc phase content at 500-620 °C		X			X	X	
5m – AW	Initial state	x	x	x		x		
MMA, P91	STCT – 620 °C/170/112 h (fr)		x		(x)		x	
	ACT – 620 °C/38.0 ksec (fr)		x				x	Z
6m – HT	Initial state		x				x	
MMA, P91	STCT – 620 °C/130/282 h (fr)		x	x		x	x	
	ACT – 620 °C/51.3 ksec		x			x	x	
5m & 6m	Thermocalc phase content at 500-620 °C		X			X	X	L
5s – AW	Initial state		x				x	
MMA, P91	STCT – 620 °C/130/381 h		x				x	L
	ACT – 600 °C/26.6 ksec		x			x	x	
8s – HT	STCT – 620 °C/130/31 h		x				x	
MMA, P91	ACT – 600 °C/24.5 ksec		x		(x)	x	x	L
5s & 8s	Thermocalc phase content at 500-620 °C		X			X	X	(L)
10s – HT	Initial state		x		x		x	
MMA, P91	ACT – 600 °C/82.6 ksec		x			x	x	Z
10s	Thermocalc phase content at 500-620 °C		X			X	X	

(x) – minor amounts of phases found on thin foil specimens in TEM.
(fr) – carbon extraction replicas taken from fractures of samples.
(L) – Laves phase appearing only in a part of the mentioned range.

What follows are the examples of microstructures observed before and after the creep tests.

4.1 Microstructures of P91 MMA weld metals 5m and 6m

4.1.1 Weld metal 5m in initial as-welded state

This microstructure is low-carbon martensitic, Figure 41, with characteristic substantial micro-inhomogeneity; an example in Figure 42 shows pseudo-twinned fine martensite laths next to coagulated small carbides and a ferrite grain with very high density of dislocations. Such ferrite grains with high dislocation density are usually of 1-3 μm sizes. In this microstructure chains of carbides (mainly cementite) appear at bottoms of columnar crystals (Figure 43) i.e. close to inter-bead heat-affected zones. Due to the very high dislocation density in the ferrite / martensite grains and related high diffraction contrast, these precipitates can be better visualised in carbon extraction replicas, Figure 44, than in thin foil TEM specimens.

The cementite precipitates at the bottoms of columnar crystals, which are tracing the former austenite grain

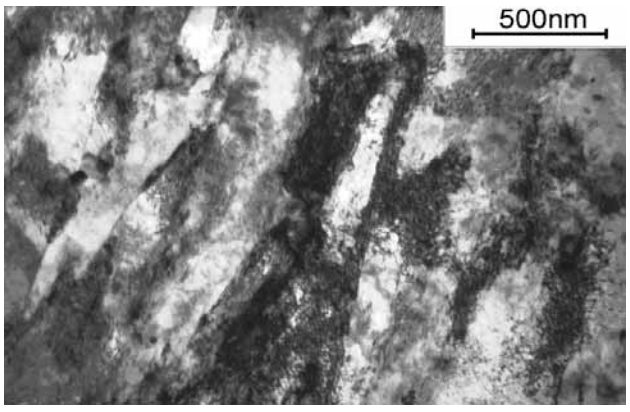

Figure 41 – Low-carbon martensitic acicular microstructure of as-welded P91 MMA weld metal

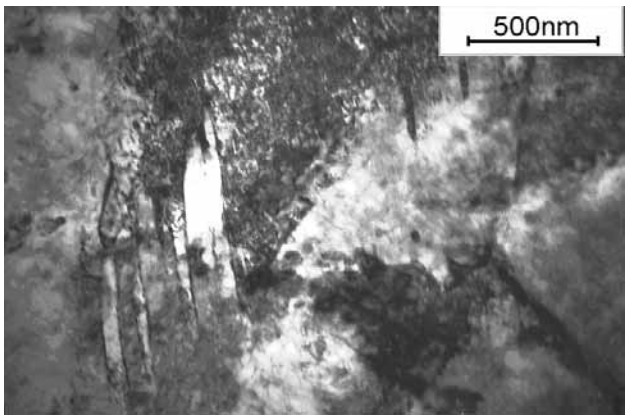

Figure 42 – Nano-twinned martensite next to granular carbides in as-welded P91 MMA weld metal

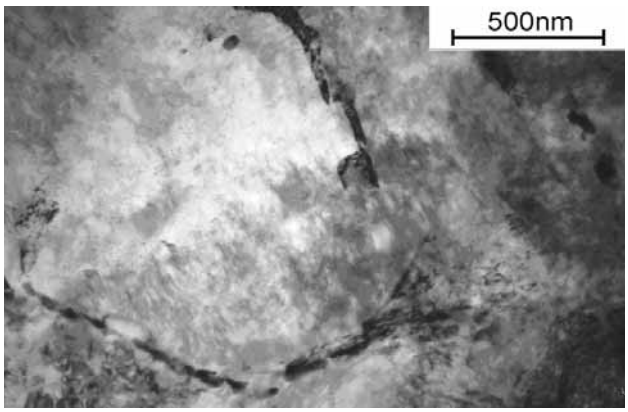

Figure 43 – Chains of cementite along ferrite grain boundaries at roots of columnar crystals in as-welded P91 MMA weld metal

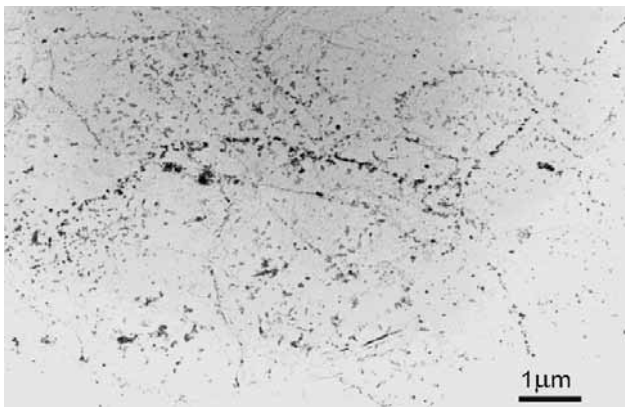

Figure 44 – Carbon extraction replica from region like in Figure 43, showing size and distribution of carbides

boundaries and the present martensite lath boundaries are Cr-rich and have average particle sizes of approx. 100 nm. In the inter-bead heat-affected zones also oval Cr-rich carbides of $M_{23}C_6$ and M_7C_3 types appear, having sizes of up to 120 × 30 nm (Figure 44). Very fine particles (5-10 nm) with the Cr:Fe ratio 3/2 were found inside the grains surrounded by the chains of the larger (cementite) particles. In these IBHAZ (inter-bead heat-affected zones) chains of somewhat smaller carbides appear also along martensite lath boundaries.

4.1.2 Weld metal 5m after short-term creep test (STCT)

After STCT the initial microstructure transformed visibly, although retained to a large extent its former martensitic morphology. On SEM picture of the fracture, taken after electrolytic removal of oxides, Figure 45, chains of coagulated carbides can be seen tracing ridges of large dimples of the ductile hot fracture. Longer duration electro-polishing and etching of this fracture surface reveals the microstructure retaining the post-martensitic morphology, showing the acicular features coexisting with recrystallised grains, Figure 46. For this microstructure after the STCT, the results of TEM observations on thin foils have not been available as yet. Despite this drawback, at larger magnifications available in SEM as well as on carbon extraction replicas it could be seen that the microstructure after STCT is fully recrystallised with ferrite grain sizes up to 8 µm.

The carbon extraction replicas taken from the 5 m sample after STCT show evidence of high temperability resulting in a very high-density precipitation of coagulated carbides, Figure 47. Two types of particles were identified, i.e. the Cr-rich $M_{23}C_6$ of middle size (with Cr:Fe ratio of 3/1, approx. 100 nm) and of large size (Cr:Fe 3.5/1, approx. 300 × 150 nm) as well as the very fine MX phase (of sizes 15-20 nm), like given in Figure 48.

4.1.3 Weld metal 5m after accelerated creep test (ACT)

Also after the ACT the microstructure is fully recrystallised, with grain size between 10-15 µm and with coagulated particles densely precipitated on former austenite grain boundaries as well as on grain boundaries of recrystallised ferrite. When observed in SEM at

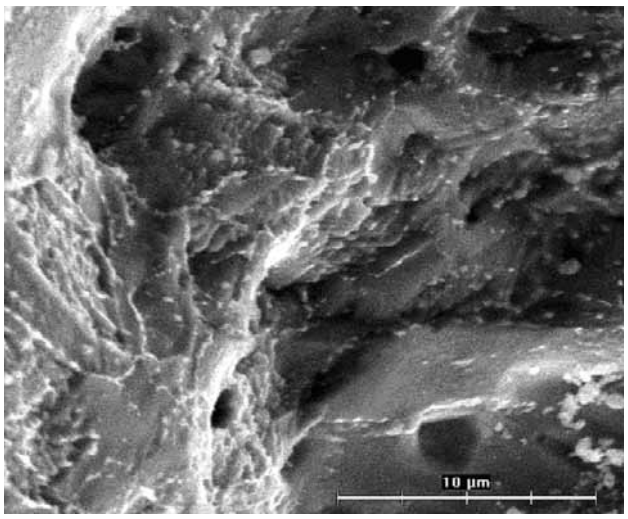

Figure 45 – Chains of coagulated carbides tracing ridges of dimples on fracture of STCT sample; P91 weld metal 5m

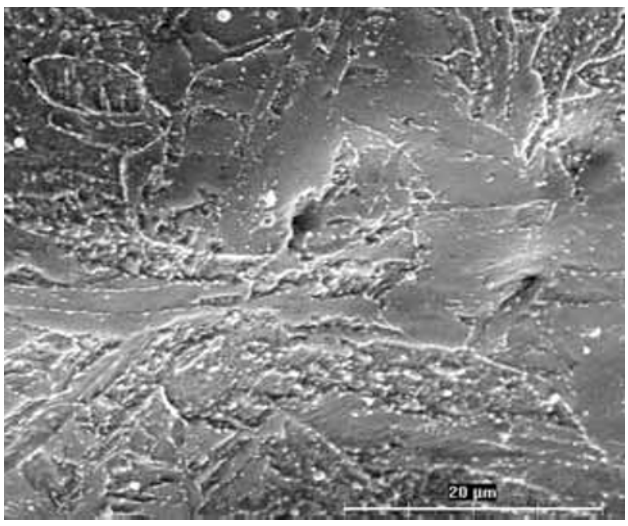

Figure 46 – Electropolished and etched fracture surface of STCT sample 5m, showing retained post-martensitic microstructure

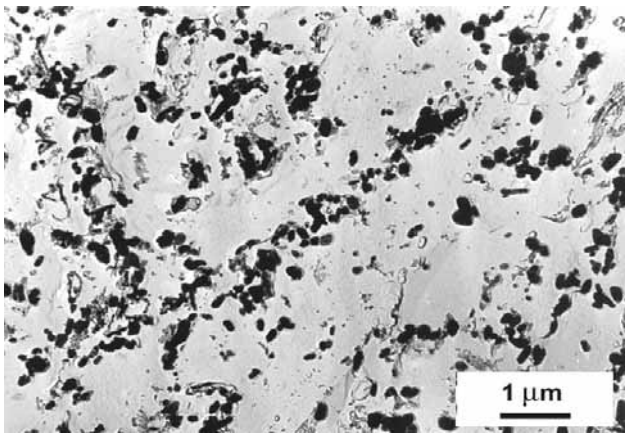

Figure 47 – High density agglomerates of coagulated carbides extracted on carbon replica from STCT sample 5m

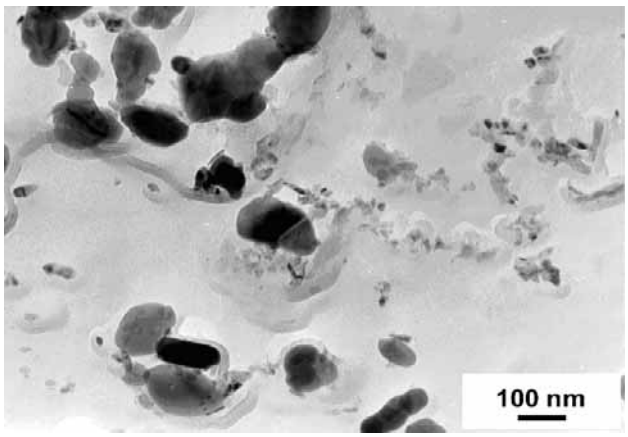

Figure 48 – Enlarged detail of Figure 47, showing medium size $M_{23}C_6$ carbides as well as very fine particles of MX phase

low magnification, this microstructure shows a post-martensitic morphology, Figure 49, while at larger magnifications the sizes and distribution of carbides can be seen in more detail, Figure 50. In carbon extraction replicas two types of particles were identified, i.e. the Cr-rich $M_{23}C_6$ (of Cr:Fe ratio 3.9/1, and size approx. 120 nm) and very fine MX (sizes up to 15 nm), Figure 51.

In the recrystallised ferrite matrix small grains and subgrains dominate, Figure 52, and the subgrains sizes reach 1.5 µm. Most of the subgrain boundaries are well defined and along them chains of carbides appear, Figure 53, while inside the subgrains very fine precipitates can be seen. Many of these fine grains and subgrains contain recovered configurations of dislocations,

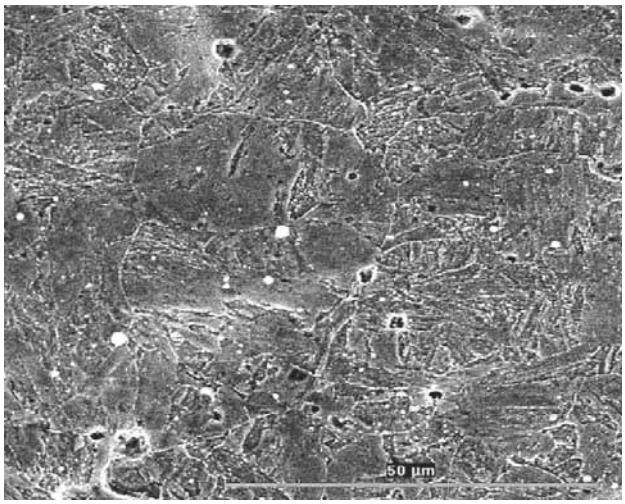

Figure 49 – Post-martensitic microstructure near to fracture surface after ACT in P91 sample 5m

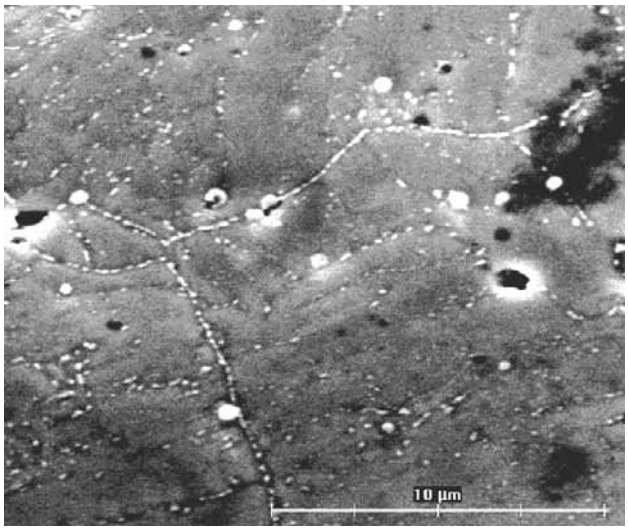

Figure 50 – Chains of carbides, inclusions and creep voids near to fracture surface in ACT sample 5m

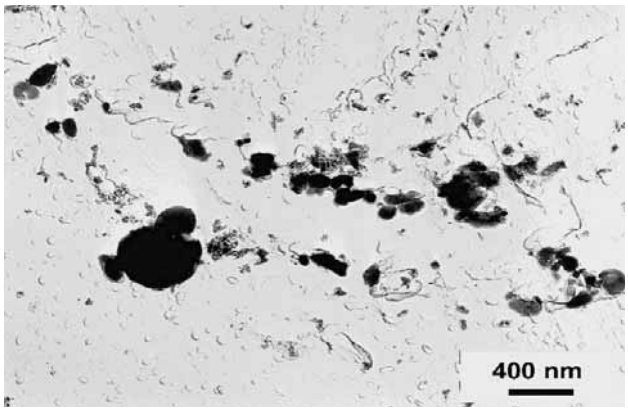

Figure 51 – Carbon extraction replica showing medium-size $M_{23}C_6$ carbides and fine MX phase particles after ACT in sample 5m

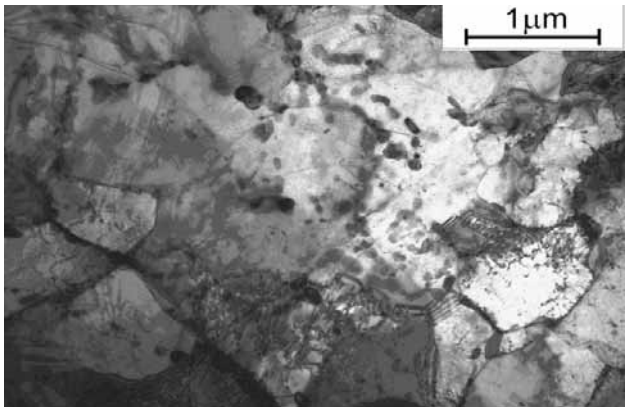

Figure 52 – Recrystallised ferrite grains and subgrains with chains of carbides after ACT in sample 5m

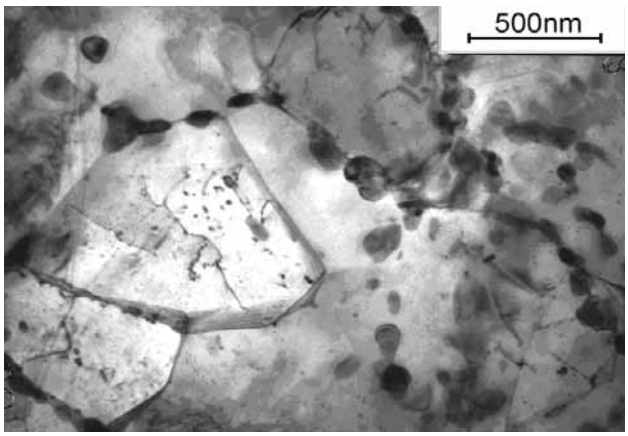

Figure 53 – Recovered subgrains with few MX particles inside and chains of coagulated $M_{23}C_6$ carbides after ACT in sample 5m

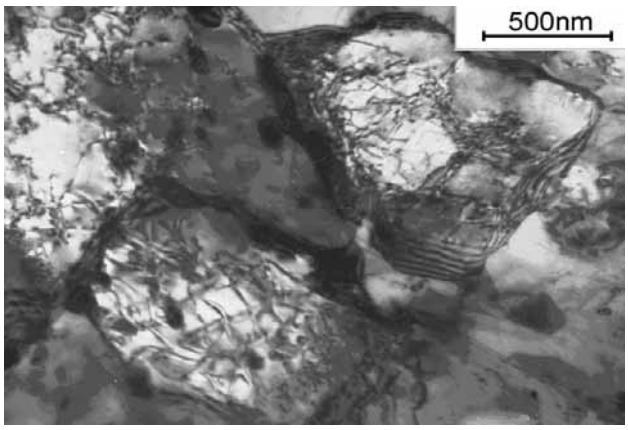

Figure 54 – Medium-density dislocation configurations in recovered subgrains after ACT in sample 5m

forming low angle boundaries, Figure 54, and formation of larger recrystallised grains occurs by coalescence of the subgrains associated with dissipation of these low angle boundaries.

4.1.4 Weld metal 6m in initial PWHT state

The PWHT caused decomposition of former martensite to the ferrite + carbide mixture, Figures 55 and 56. Some of the recrystallised grains and subgrains retain the post-martensitic orientation and accordingly carbides along their boundaries form oriented arrays, Figure 56. In inter-bead heat-affected zones, the microstructure consists of small subgrains (of approx. 0.5 μm) filling-in former austenite grains surrounded by secondary particles, Figure 57. Somewhat larger subgrains of slightly elongated form appear in former martensite laths, Figure 58. Among the particles after the PWHT the following dominate: $M_{23}C_6$ (Cr:Fe 2.5/1, up to 350 × 200 nm); and MX (approx. 20 nm).

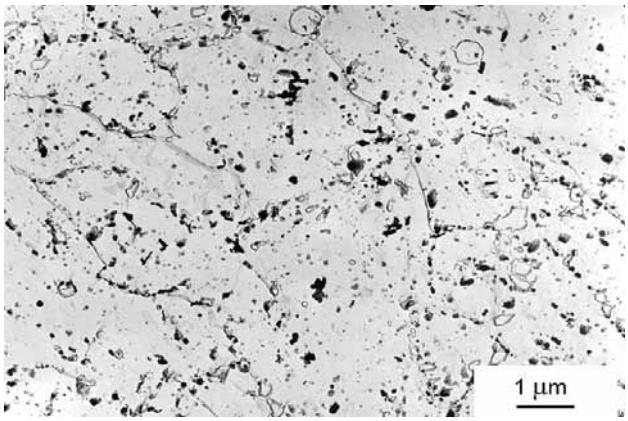

Figure 55 – Carbide size and distribution of inter-bead heat-affected zone in high-tempered P91 weld metal sample 6m

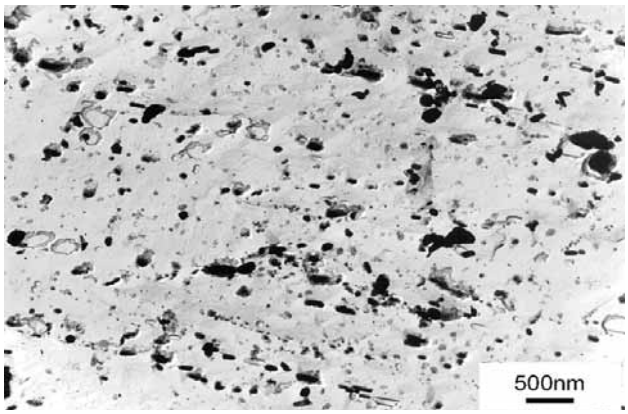

Figure 56 – Arrays of carbides in high-tempered martensite microstructure of former columnar crystals in sample 6m

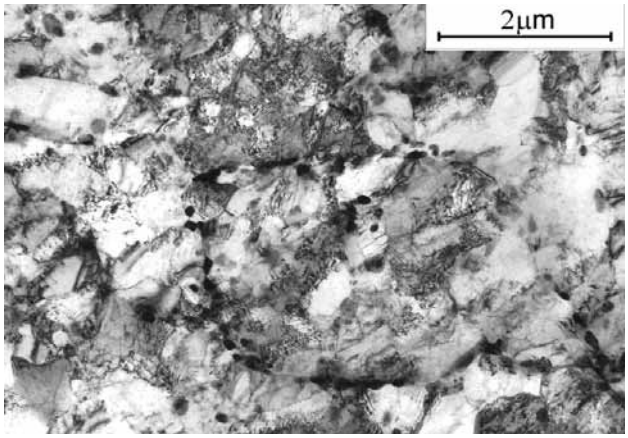

Figure 57 – Microstructure of high-tempered sample 6m consisting of recovered ferrite subgrains and coagulated carbides

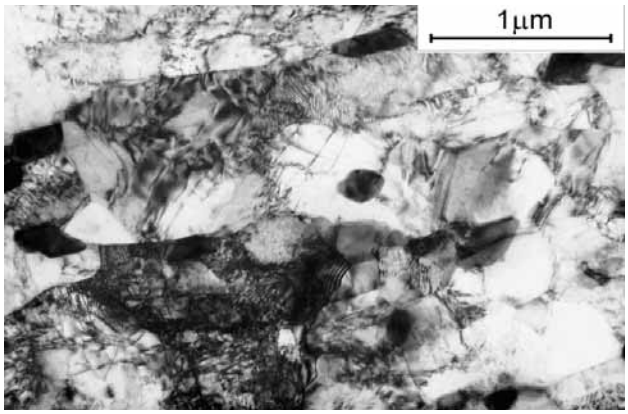

Figure 58 – Recovered ferrite subgrains retaining orientation of post-martensitic laths in P91 weld metal sample 6m

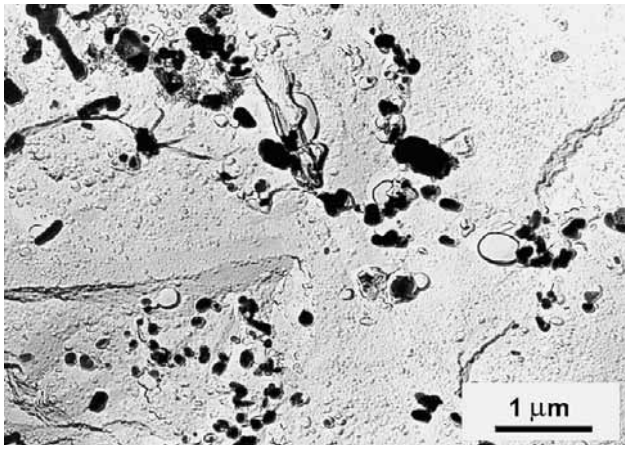

Figure 59 – Medium-size $M_{23}C_6$ carbides and fine MX precipitates in recrystallised ferrite matrix after STCT of sample 6m

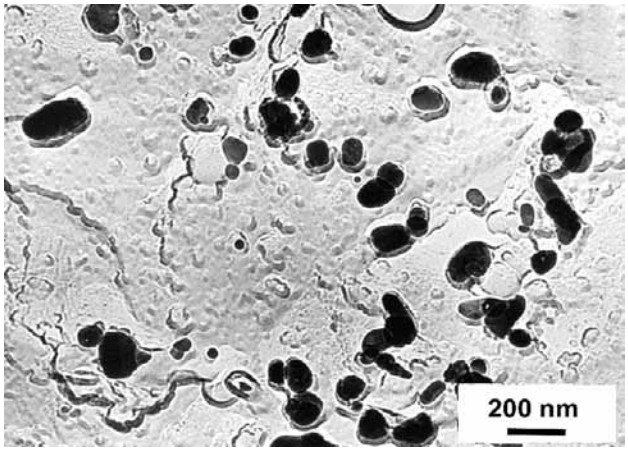

Figure 60 – Enlarged fragment of Figure 59 showing a colony of ~ 100-200 nm size MX particles in sample 6m after STCT

4.1.5 Weld metal 6m after short-term creep test (STCT)

The microstructure after STCT is fully recrystallised with grain size 3-7 μm, Figures 59 and 60. The recrystallised ferrite grains are decorated with strings of Cr-rich $M_{23}C_6$ carbides having Cr:Fe ratio 2/1 (sizes up to 200 $\times$100 nm) and 1.2/1 (up to 120 $\times$ 80 nm). For intragranular areas, dense precipitation of very fine MX particles (up to 10 nm) has been typical. The early stage of M_6C precipitation was also observed (20-30 nm i.e. very small particles).

Thin foil specimens for TEM observations of substructure were not yet prepared from this state. This part of the work is still in progress.

4.1.6 Weld metal 6m after accelerated creep test (ACT)

On fracture surfaces of ACT samples, after electrolytic removal of oxides, deep ductile voids could be observed as well as networks of coagulated medium-size carbides, Figure 61.

At about 1 mm from the fracture surface the recrystallised microstructure has the grain size of approx. 10 μm and subgrain size approx. 2 μm. In this post-martensitic microstructure, the boundaries of former laths are covered with higher density of the secondary particles, Figure 62. Altogether two types of particles were identified in ACT specimens: $M_{23}C_6$ carbides (Cr:Fe 2.3/1, 100 $\times$ 80 nm, rarely 400 $\times$ 200 nm) located along the boundaries and fine- and medium-size MX (20 $\times$ 10 nm and 80 $\times$ 20 nm, respectively) appearing along the boundaries of the former laths as well as inside the recrystallised grains and subgrains.

This microstructure, when observed in TEM on thin foils specimens, reveals recrystallised ferrite grains containing networks of recovered dislocations interacting with fine carbides, Figure 63. The recrystallisation of ferrite, by coalescence of subgrains and by annihilation of smaller grains, proceeds in such a way that chains and colonies of carbides, which certainly earlier precipitated along the martensite lath boundaries or similar interfaces, are no more at such locations as these boundaries evidently migrated away from them, Figure 64.

4.2 Microstructures of P91 MMA weld metals 5s and 8s

4.2.1 Weld metal 5s in initial as-welded state

The microstructure of this MMA P91 weld metal in the as-welded state is generally acicular low-carbon marten-

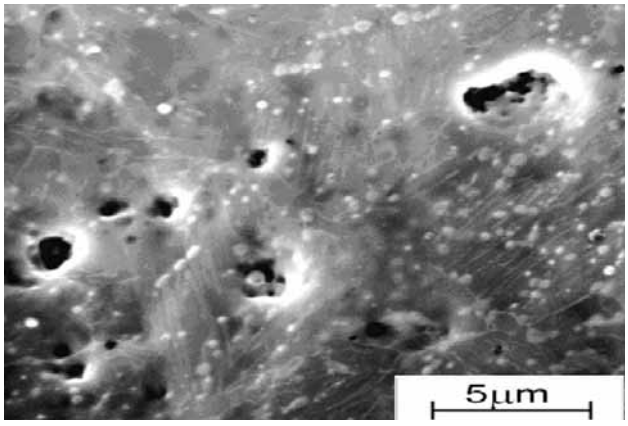

Figure 61 – Deep ductile voids and coagulated carbides at fracture surface of AC tested sample 6m

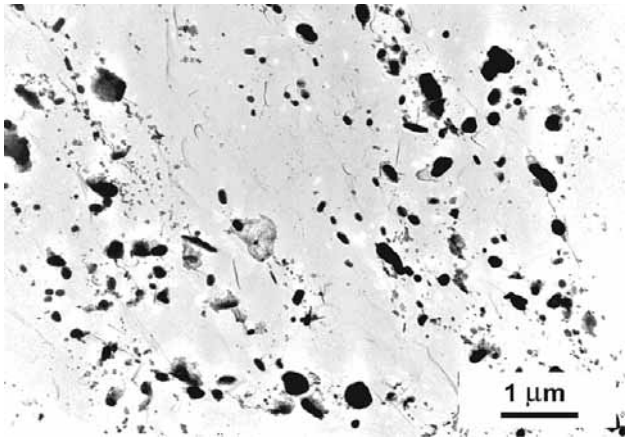

Figure 62 – Coagulated carbides in post-martensitic microstructure of sample 6m at about 1 mm from ACT fracture surface

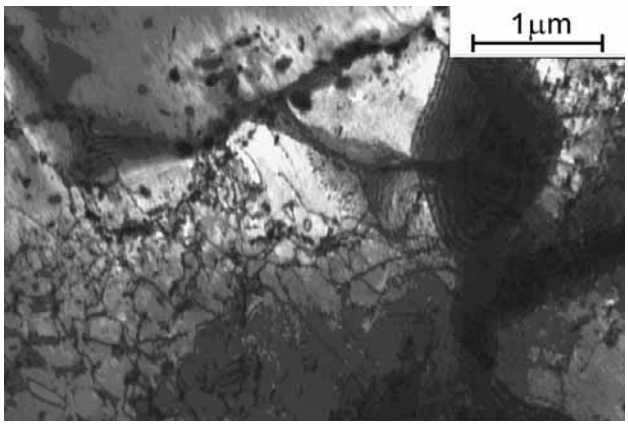

Figure 63 – Recrystallised ferrite containing network of dislocations interacting with fine carbides in sample 6m after ACT

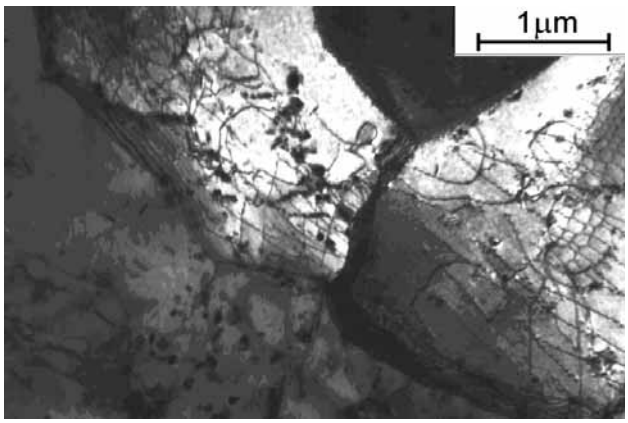

Figure 64 – Arrays of carbides in recrystallised ferrite grains in sample 6m after ACT

sitic with high density of tangled dislocations (Figure 65) in the martensite laths. It contains spheroidal inclusions of sub-micron size. In inter-bead heat-affected zones (IBHAZ) chains of particles are visible along former boundaries of austenite grains (Figure 66).

The former austenite grain boundaries and the martensite lath boundaries, like in Figure 67, are decorated with middle-sized (80 $\times$ 50 nm) Cr-rich $M_{23}C_6$ particles having Cr/Fe ratio of 1.7/1. Inside the martensitic laths very fine MX particles in limited quantity were found (see Figures 67 & 68).

4.2.2 As-welded weld metal 5s after short-term creep test (STCT)

The STCT caused transformation of the initial (as-welded) microstructure, i.e. recovery and recrystallisation of the martensitic matrix and precipitation of carbides. The intensity of the transformation depends on the local strain; it is more intensive in the necked portion of the STCT sample (Figure 69) and less intensive in the uniformly strained “stem” portion (Figure 70), as visible on the SEM metallographic images. Here some deformation / elongation of recrystallised grains can be seen

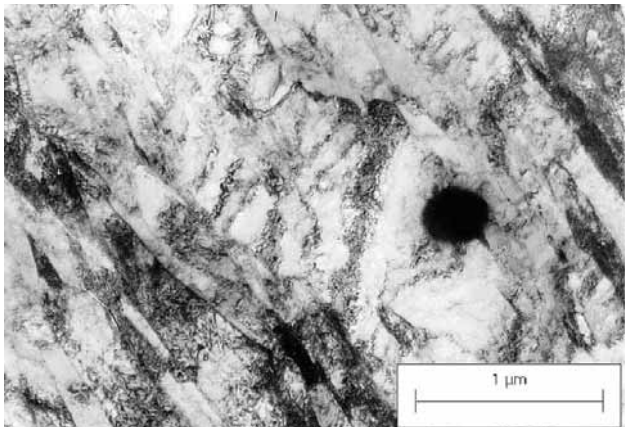

Figure 65 – Martensitic microstructure of as-welded sample 5s

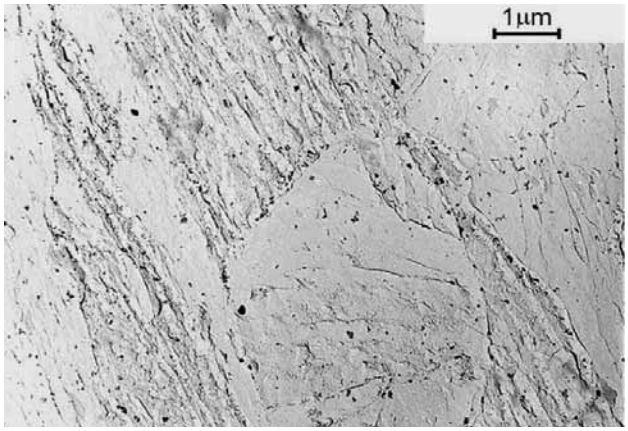

Figure 66 – Carbon extraction replica of sample 5s showing fine precipitates in martensite

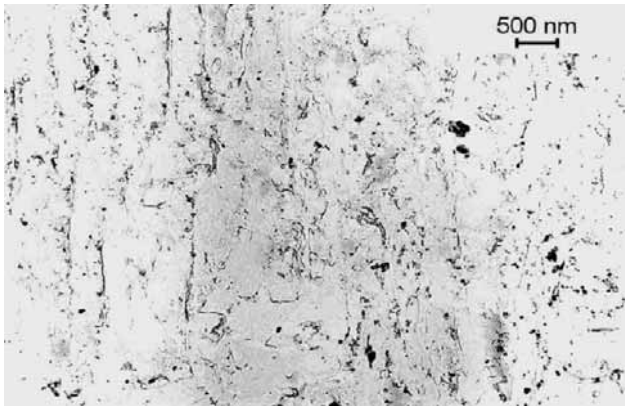

Figure 67 – Heat-affected region of sample 5s with medium-sized $M_{23}C_6$ carbides and very fine MX particles

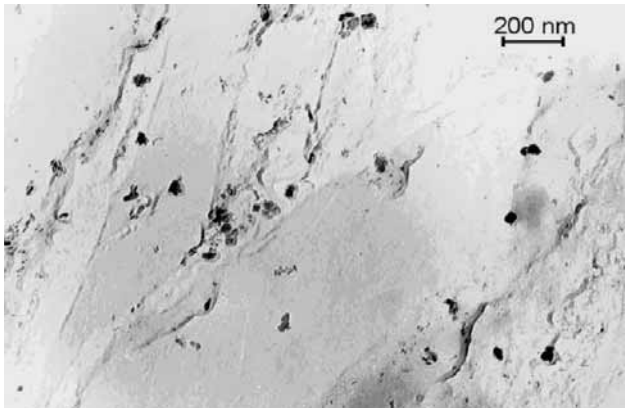

Figure 68 – Microstructure as in Figure 67 showing the carbides in martensite laths

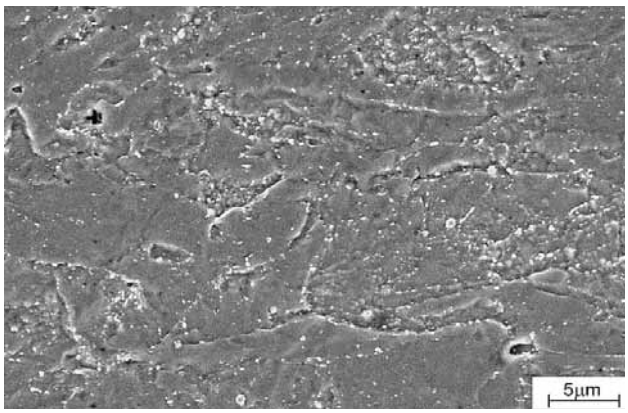

Figure 69 – Transformed microstructure of necked portion of STCT sample 5s

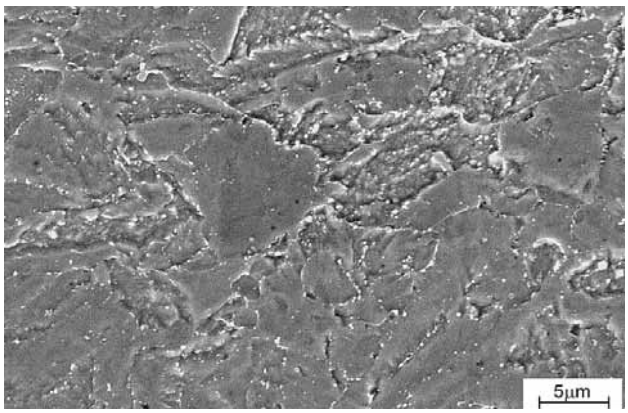

Figure 70 – Post-martensitic microstructure of uniformly strained "stem" portion of STCT sample 5s

in the neck portion (Figure 69). When observed at larger magnification on carbon extraction replica (Figure 71), the fine grains / subgrains, dominating in the neck portion of the STCT sample appear surrounded by chains of larger-than-average carbides. Majority of the particles comprise Cr-rich $M_{23}C_6$ carbide. As compared with the as received state, these particles are larger (up to 200 nm) with higher chromium content (Cr/Fe ratio 3.5/1). Only seldom were larger Laves phase found as well as very fine MX particles (Figures 71 & 72), usually in the stem portion of the sample. The larger particles are predominantly situated along all kinds of boundaries, whereas fine particles precipitate inside the grains and laths.

This microstructure, when observed by TEM on thin foils reveals advanced recrystallisation in the equiaxed small grains dominating in the neck portion of the STCT sample (Figure 73). In the stem portion of this sample, the characteristics of the prior lath martensitic microstructure are retained. In these areas the recrystallisation of the matrix evidently occurs by coalescence of subgrains while the chain-like arrays of carbides retain their former orientations along the prior martensite lath boundaries (Figure 74), thus crossing the recrystallised (ferrite) grains.

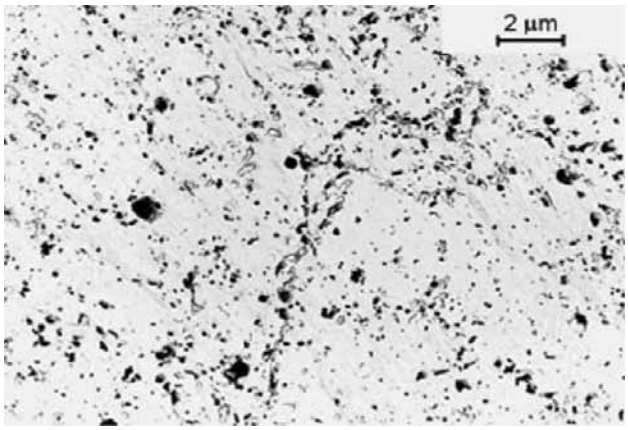

Figure 71 – High density of medium-sized $M_{23}C_6$ carbides in the necked portion of STCT sample 5s

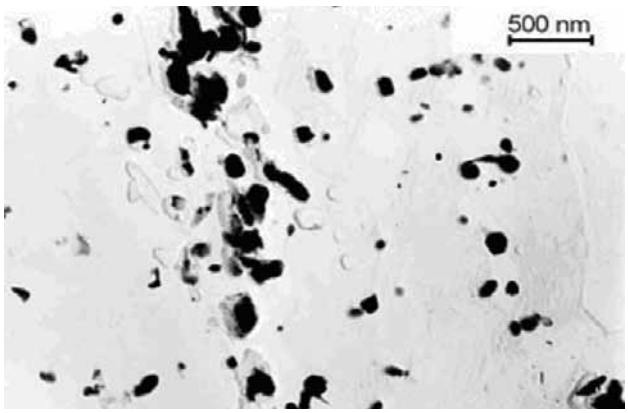

Figure 72 – Microstructure of STCT sample 5s showing colony of medium-sized $M_{23}C_6$ carbides at grain boundary

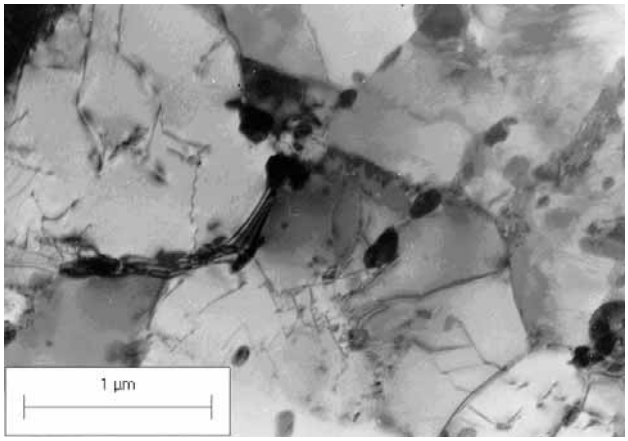

Figure 73 – Equiaxed small grains formed in the neck portion of sample 5s after STCT

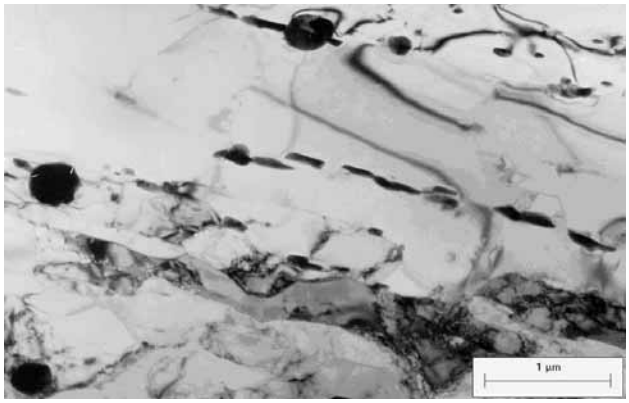

Figure 74 – Elongated post-martensitic grains dominating in the stem portion of sample 5s after STCT

4.2.3 As-welded weld metal 5s after accelerated creep test (ACT)

The ACT also results in transformation of the matrix and intensive precipitation of carbides. Sizes and distribution of partly spheroidised larger carbides can be seen on SEM images, like in Figure 75. Fine, well recovered subgrains and grains of sizes about 1-2 μm formed in the matrix near "triple-points" of the former austenite grains, Figure 76, where also larger than average carbides appear. Chains of the larger carbides as well as their agglomerates can be observed along these former austenite grain boundaries.

Recrystallised ferrite grains of 5 μm or larger sizes form by coalescence of fine subgrains, Figure 77, and often contain medium-density configurations of tangled dislocations interacting with very fine precipitates. The subgrains of < 1 μm size have dislocation-type low angle boundaries and retain orientation of the former martensite laths, especially when the fine precipitates visible in these subgrains remain in arrays following the directions of former inter-lath boundaries of the martensite (Figure 78).

As this particular specimen after ACT (5s) was not made available in a proper time for taking carbon extraction replicas and identifying carbides on the replicas, more attention was put here on identifying the carbides using selected-area electron diffraction.

It was found that the largest carbides observed by SEM metallography and also visible in TEM on thin foil specimens as distributed along ferrite grain boundaries / former austenite grain boundaries (Figures 76 & 77), were mainly of $M_{23}C_6$ type, although some M_6C carbides could be identified as well, like the one pinning the grain boundary in Figure 79.

As to the precipitates dominating within the recovered post-martensitic subgrains, these were positively identified as mainly of cubic MX type (the finest ones) and some of them as hexagonal M_2X type (the elongated ones), Figure 78. Some fine M_7C_3 carbides were found too, like these showed near to the ferrite grain boundary in Figure 80.

4.2.4 Post-weld heat-treated weld metal 8s after short-term creep test (STCT)

STCT causes further tempering of the microstructure. Localised strain in the neck portion contributes to the formation of fine well recrystallised equiaxed grains and subgrains, the last of sizes less than 1 μm, Figure 81, appearing mainly at triple points of former austenite grains, where also colonies of coagulated carbides could be seen. Inside the former austenite grains, elongated subgrains retain the post-martensitic orientation and so do the carbides, Figure 82. Such distribution of carbides could be also seen on carbon extraction replicas,

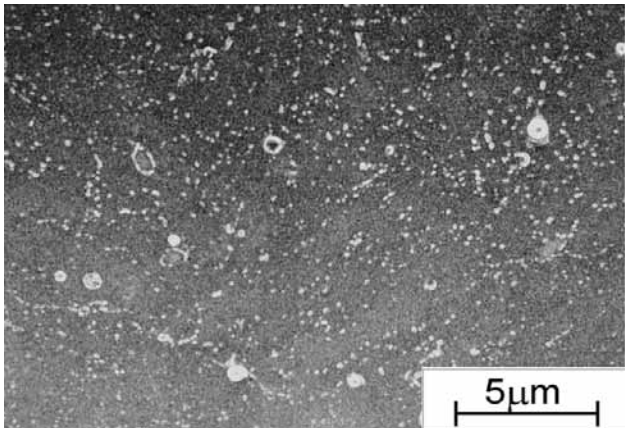

Figure 75 – Distribution of spheroidised carbides in 5s sample after ACT

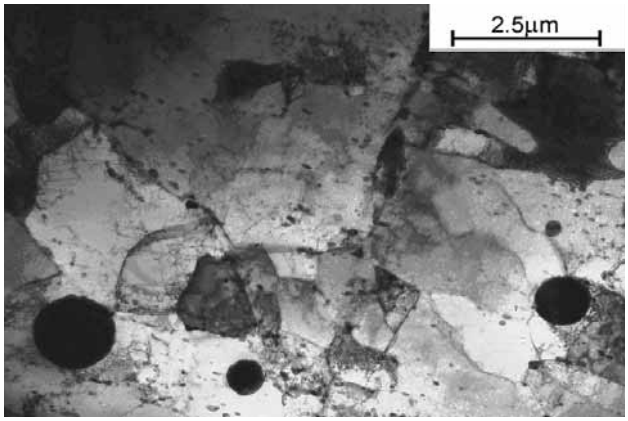

Figure 76 – Fine recrystallised grains and subgrains in sample 5s after ACT

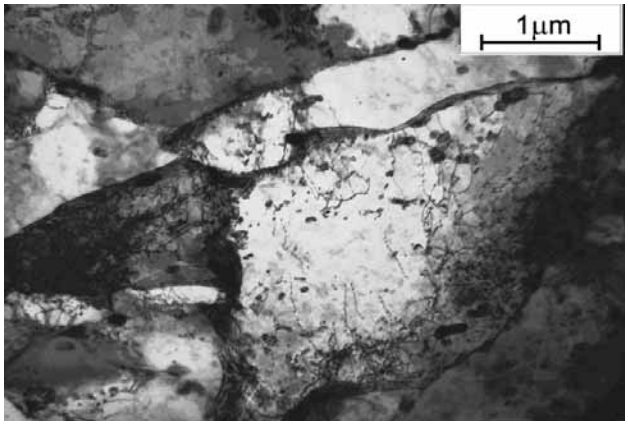

Figure 77 – Recrystallised ferrite with numerous tangled dislocations in sample 5s after ACT

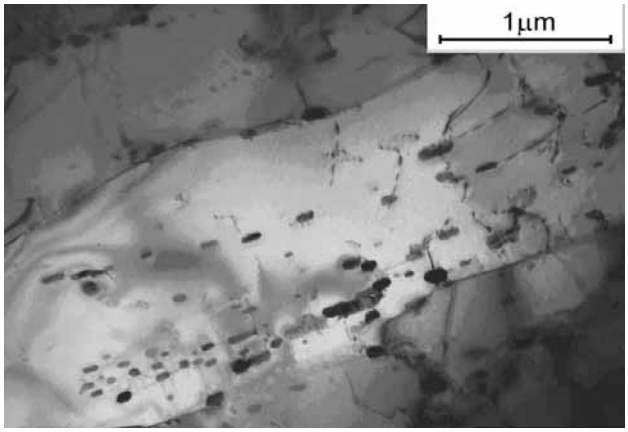

Figure 78 – Carbides retaining orientation of martensite laths in sample 5s after ACT

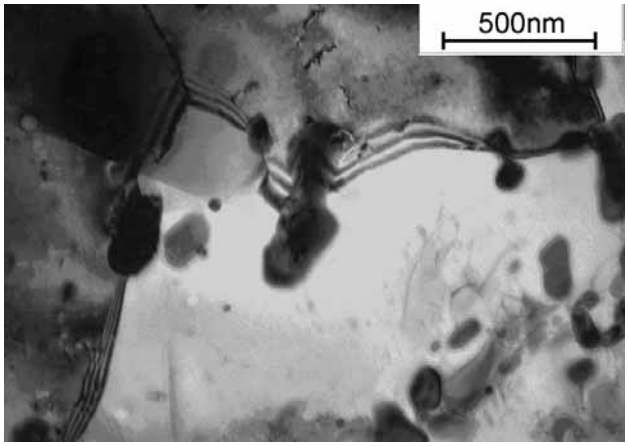

Figure 79 – M_6C carbide pinning ferrite grain boundary in sample 5s after ACT

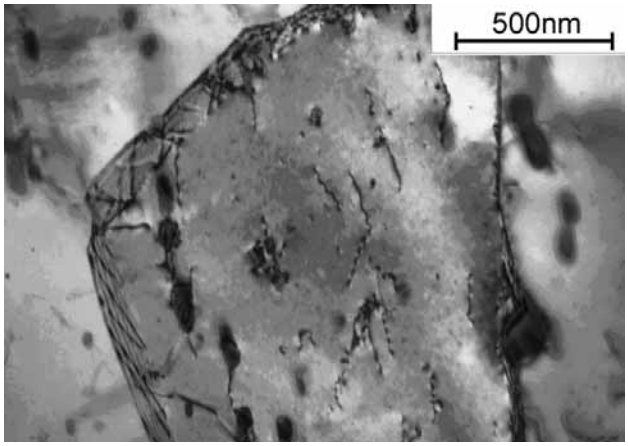

Figure 80 – Elongated M_7C_3 carbides found in a small subgrain in sample 5s after ACT

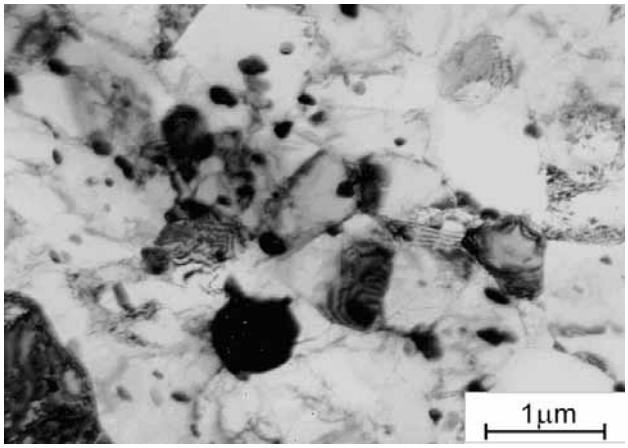

Figure 81 – A colony of carbides and fine subgrains of ferrite in neck portion of STCT sample 8s

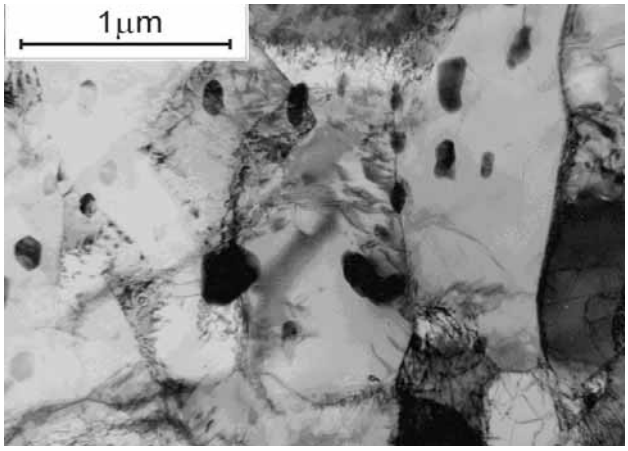

Figure 82 – Elongated ferrite subgrains dominating in stem portion of sample 8s after STCT

Figures 83 to 86, used for identification of the carbides. The carbides dominating after STCT are Cr rich (Cr:Fe 3/1) with the size up to 200 × 150 nm, predominantly approx. 80 nm.

Several randomly distributed MX particles with 100 nm average size were also found. In the stem portion of the STCT sample, the recrystallised grains and subgrains were larger than in the necking portion, i.e. grains up to 4 μm and subgrain size up to 1.5 μm, Figures 87 & 88.

Here, many of these recrystallised grains were elongated in the direction of former martensite laths, Figures 86 & 88, and inside these grains only very few fine precipitates could be seen.

4.2.5 Post-weld heat-treated weld metal 8s after accelerated creep test (ACT)

On electro-polished and etched fracture surface of ACT sample two kinds of carbides are visible – the larger

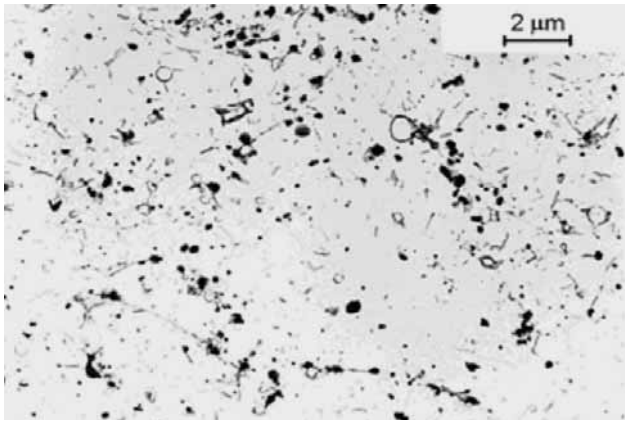

Figure 83 – Distribution of carbides in stem portion of sample 8s after STCT

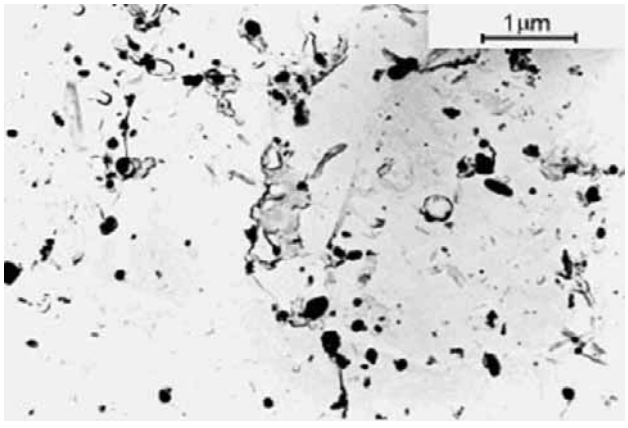

Figure 84 – Medium-sized $M_{23}C_6$ carbides and fine MX particles in neck portion of sample 8s after STCT

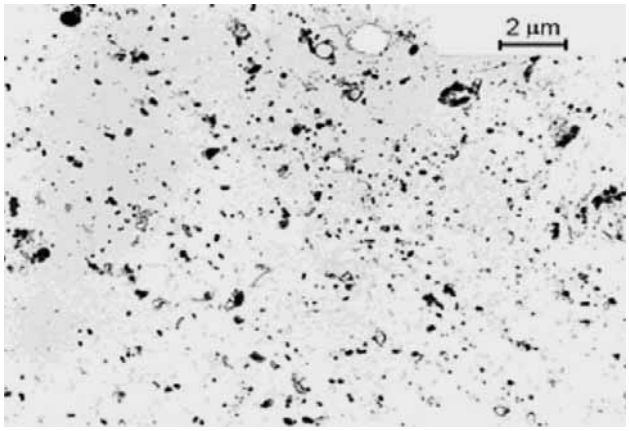

Figure 85 – Distribution of carbides in neck portion of sample 8s after STCT

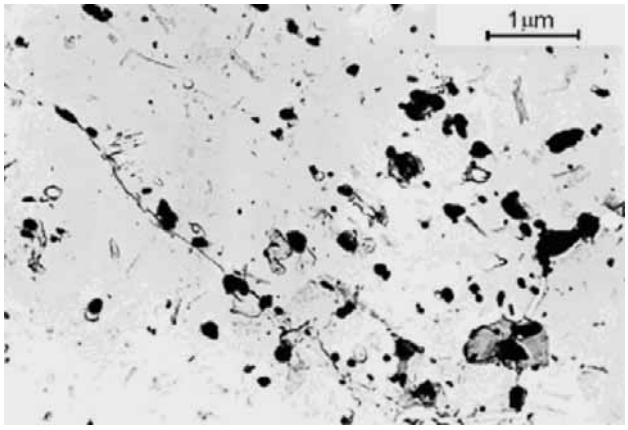

Figure 86 – $M_{23}C_6$ carbides distributed along former martensite lath boundaries in stem portion of sample 8s after STCT

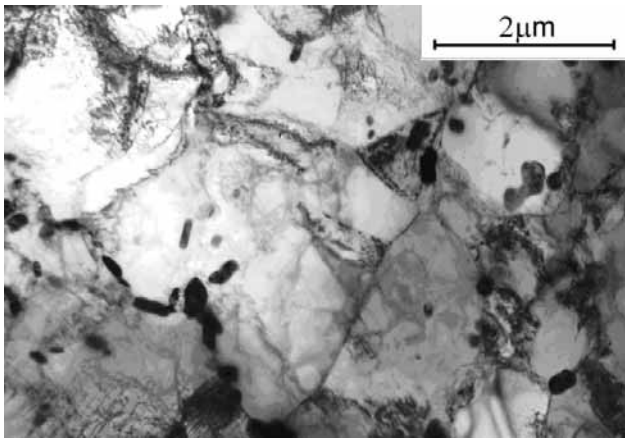

Figure 87 – Equiaxed grains and subgrains in neck portion of sample 8s after STCT

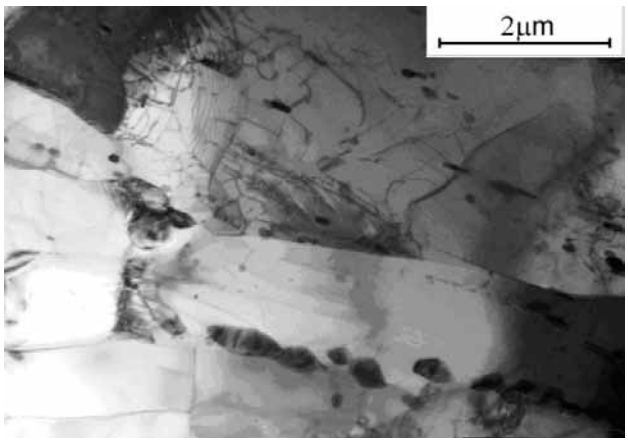

Figure 88 – Elongated recrystallised ferrite grains in stem portion of sample 8s after STCT

ones tracing grain boundaries of recrystallised ferrite and the smaller present-in the ferrite grains (Figure 89). The average grains of the recrystallised ferrite are approx. 3 µm in size while the subgrain sizes vary between 0.5-1 µm. The larger carbides extracted in carbon replicas (Figure 90) appeared to be mainly of $M_{23}C_6$ and less of M_6C types, while the very fine ones were identified as M_2X and MX. The M_6C carbides often formed dense colonies at "triple-points" between recrystallised ferrite grains (Figure 91). Somewhat smaller colonies of $M_{23}C_6$ and M_6C (having particle sizes up to 500 × 200 nm) appear at ferrite grain boundaries, Figure 92, while inside these ferrite grains the M_2X (50 × 10 nm, Figure 93) and MX (approx. 15 nm, Figure 94) particles are pinning recovered dislocations. Laves phase particles of 100 nm sizes were found on some ferrite grain boundaries as well.

Characteristic of this 8s MMA weld metal has been its micro-scale inhomogeneity certainly originated from as-welded state and retained after PWHT, so that the accelerated creep test produced the dense colonies of coagulated carbides at the "triple-point" sites while interiors

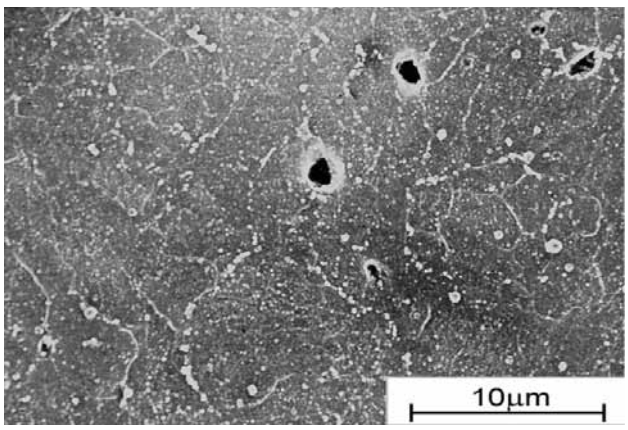

Figure 89 – Distribution of carbides near fracture surface in sample 8s after ACT

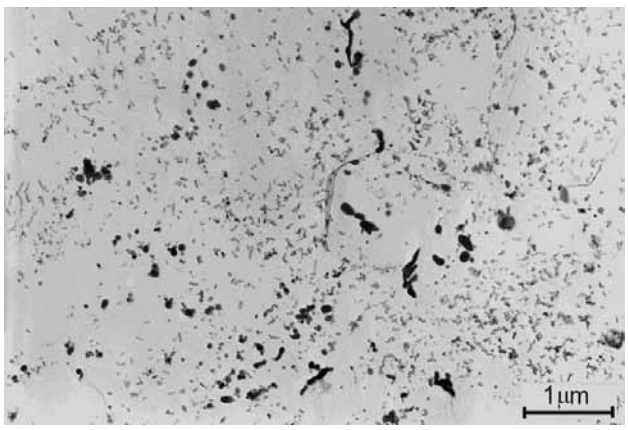

Figure 90 – Carbides extracted on carbon replica from fracture surface of sample 8s after ACT

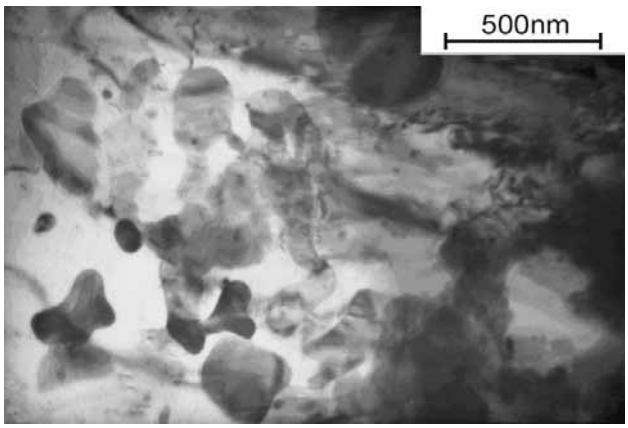

Figure 91 – A colony of M_6C carbides near "triple point" of the ferrite matrix in sample 8s after ACT

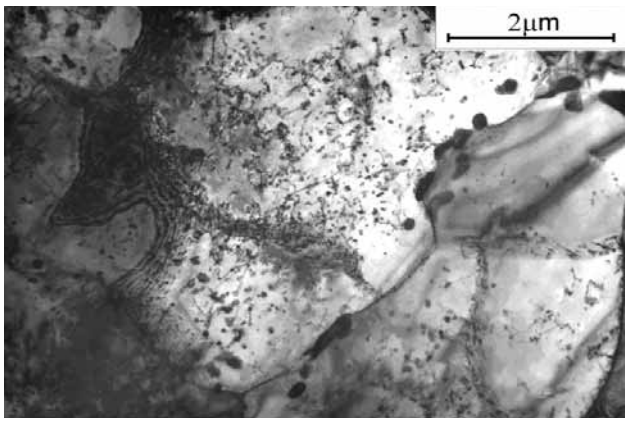

Figure 92 – Fine MX and M_2X precipitates pinning dislocations in ferrite of sample 8s after ACT

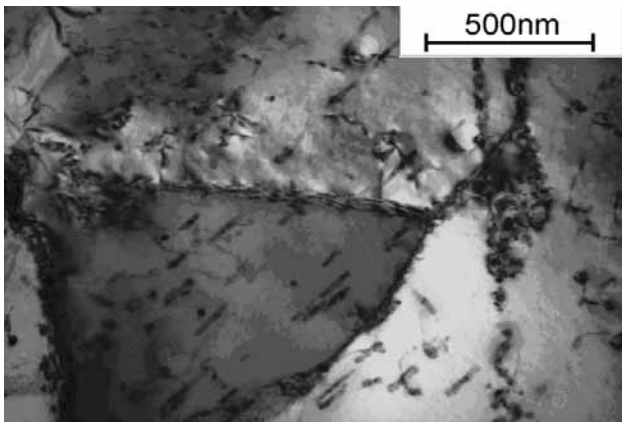

Figure 93 – M_2X precipitates in recrystallised ferrite grains in 8s after ACT

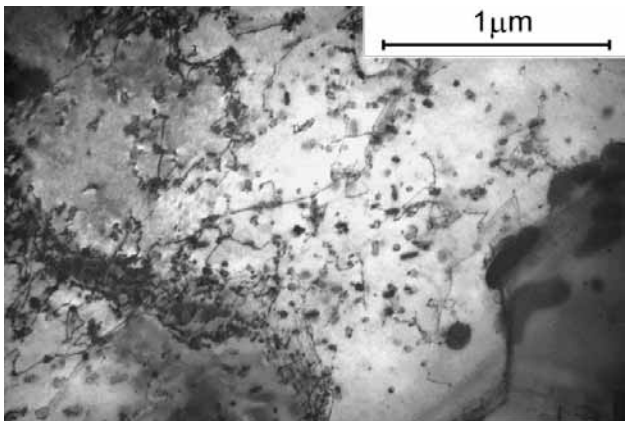

Figure 94 – Fine MX precipitates interacting with dislocations in ferrite of sample 8s after ACT

of recrystallised grains were still filled in by numerous very fine precipitates evidently interacting with dislocations.

5 DISCUSSION

In the presented here part of the work two MMA P91 weld metals are compared. Results obtained for other creep-resisting weld metals in the SmartWeld project and in its follow-up will be presented in further reports.

The principal concept of the SmartWeld EU project was a "smart" welding consumable design which deposits a relatively weak but strain-hardening weld metal, and thus achieves good high temperature properties accompanied by low welding residual stresses. A parallel concept was the need to develop weld metals, which match the high temperature properties of the parent materials to be welded. From this point of view the composition of 5m & 6m consumable, and its welding plus treatment, allowed to obtain a product of initial martensitic / ferritic microstructure having high hot strength and high temperability. Then the 5s & 8s composition was successful for manufacturing a medium strength strain-hardening weld metal of initial bainitic / martensitic microstructure and then optimizing its treatment for maximum of creep life.

The reference material – the crept component: antler-weld-stub, which was in operation until the end of its life, showed highly transformed microstructure in all of its parts. Here, the absence of creep voids in the stub component could be correlated to finer initial austenite grain size and to chemical composition resulting in higher final hardness, although more advanced coalescence of carbides was observed in it.

As regards the weld between stub and antler, no creep voids could be found in its inner / steam-side bead while the voids appeared in the outer / gas-side bead. According to the supplier of the component, no temperature gradient appeared across the wall during operation and therefore the initial coarser columnar microstructure of this bead plus tensile operational stresses might be responsible for its earlier failure. While the parent materials of the stub and antler were to a large extent fully transformed and recrystallised, the weld metal between them retained many post-martensitic features resulting from its generally inhomogeneous nature.

The creep voids, appearing in the exploited component, were always nucleating in characteristic sites – along the prior austenite grain boundaries – the sites where large carbides or colonies of carbides did form. However, these preferential locations for the creep voids nucleation could never be observed in any tensile-rupture / short-term creep tested (STCT) sample of the parent materials, like these of P91 – KA817 series, as well as

in the STCT samples of the P91 MMA weld metals 5m & 6m and 5s & 8s. Much more accurate generation of the creep-like voids could be achieved in the simulative ACT on Gleeble.

Here the first comparison might be done of the STCT and ACT results on the P91 KA817 series parent material. The transformation of microstructure till fracture after the ACT at 625 °C for 28.3 ksec, very well matched this of STCT at 650 °C at 104 MPa initial stress and 969 hours to failure. And all ACT and STCT tests generated the same final phase compositions as predicted by the Thermocalc calculations. But the creep strength factors used for comparison in both tests, i.e. F_{CS} and F_{ACT} did not match so well. This discrepancy might have been due to the substantial necking of the STCT samples, certainly assisting the strain-induced precipitation in the neck portion as well as making the true stress in the STCT increasing for the unknown period of time since the crosswise reduction in area on the sample begun and finally led to the necking.

In the further testing of microstructure of the weld metal samples after STCT, it was confirmed that the microstructures of the neck portions of the samples are much more transformed than these of the uniformly strained “stem” portions. Moreover, the neck portions of STCT samples often contain much finer microstructure resulting from thermo-mechanical grain refinement during the test. No wonder, the localized or accumulated strains influenced the transformation of microstructure and precipitation processes. Not surprisingly, the recently developed simulative accelerated creep test, the ACT on Gleeble has been based on this phenomenon of accelerated precipitation induced by strains, aiming to use it in a controllable way.

All achieved results of the creep tests implemented in this work indicate sufficient microstructure transformation, i.e. the recrystallisation of matrix and formation of close to equilibrium high-alloy carbides after these tests. By Thermocalc, $M_{23}C_6$, M_6C, MX and Laves phase (plus ferrite as the matrix), have been calculated as equilibrium phases for the considered batches.

After the ACT and STCT the ferrite subgrain sizes in all examined states were between 0.5-1.5 μm. Only after the ACT in sample 6m the subgrains were a bit larger, of approx. 2 μm size; in fact these were no more subgrains as most of them possessed high-angle boundaries. The same refers to sample 8s after the ACT, in which the fine grains were of ~ 3 μm size. Evidently this refinement was due to intensive generation and annihilation of dislocations during thermal-mechanical cycles of the test. The accumulated strain of the simulative ACT also provided more nucleation sites for the grain boundary carbides, like $M_{23}C_6$ as well as enhanced strain-induced precipitation of MX and M_2X within grains. It also seemed to promote formation of clusters / colonies of medium/large size Cr-rich carbides in the materials which had been initially soft and in such state subjected to ACT, like the P91 KA817 batch and the weld metals 6m and 8s. In these last cases the carbides in the clusters were often the M_6C.

The influence of the localised strain on transformation of microstructure was also visible in STCT; here, when the necking occurs, the grain refinement in the neck portion appears as well.

The Cr-rich $M_{23}C_6$ carbides appeared dominating in STCT and ACT samples in all experimental conditions, with higher Cr:Fe ratios in the states without PWHT (up to 4/1). In the states after PWHT the Cr:Fe ratio was usually between 2.1/1 and 2.5/1. The highest Cr:Fe ratio (3.9/1) was achieved after ACT on as-welded material 5 m. Larger $M_{23}C_6$ carbide particles were present after the PWHT. Presence of high density of fine MX particles was confirmed in all test samples. M_6C carbide was seldom observed on carbon extraction replicas in the examined samples; it was however found on thin foil specimens observed in TEM, in particular after the ACT. This Mo-rich M_6C carbide practically did not precipitate before cracking of STCT samples, however it showed up after the ACT. Also another Mo-rich carbide, Mo_2C, which often precedes the M_6C precipitation, was observed in material 8s after the ACT.

Laves phase was present only after ACT in 8s batch in a low quantity; it was also found in the STCT sample 5s after a relatively long duration of the test. This could result from a small content of tungsten and a bit more of silicon in the mentioned batches.

Very fine MX particles were present in all materials in almost all states.

In general, the distribution of all fine particles was more homogenous in microstructures after the ACT. On the other hand, the largest particles, especially the colonies of carbides, were observed again after the ACT. This could have been resulting from the initial inhomogeneity of the tested weld metals and the intensification of precipitation forced by accumulated strains during the simulative accelerated creep test on the Gleeble.

It has to be mentioned in the concluding word, that the microstructure of the weld metals, especially of the multilayer multi-bead creep resisting weld metals, is much more complex than the microstructure of the parent pipe, tube or plate creep resisting steels. In particular it is inherently inhomogeneous, both chemically and metallurgically, from the beginning of testing or application till its end.

6 CONCLUSIONS

1. It has been proved in the case of creep tests, either conventional or accelerated, that localized or accumulated strains have substantial influence on the transformation of microstructure and precipitation processes.

2. The recently developed accelerated creep test (ACT) allows transforming in a relatively short time the microstructure of creep resisting steel or weldment to the stage characteristic of the long-term exploitation in the real creep conditions. The phase composition after the ACT well matches the equilibrium one calculated by Thermocalc programme.

3. The results of the ACT can be used to classify the creep resisting materials and to predict their long-term behaviour; they can be also used for providing physical data of the materials behaviour to further computer modelling as in each cycle of the ACT procedure such values like pseudo-elasticity modulus and yield strength at the test temperature are measured.

ACKNOWLEDGEMENTS

The financial support of the EU in the “SmartWeld” project: G1RD-CT-2001-00490 is here gratefully acknowledged. Cordial thanks are directed to all the partners in this project. Additionally, the authors remain very grateful to Dr. D.A. Allen from E.ON (PTC), UK, for providing the reference materials.

REFERENCES

[1] Pepe J.J., Gonyea D.C: Constant displacement rate testing at elevated temperatures, in: Fossil Power Plant Rehabilitation, ASM International, Proc Int Conf, Cincinnati OH, Feb.1989, p. 39.

[2] Mandziej S.T., Výrostková A.: Accelerated Creep Testing (ACT) Procedure for weld metals using Gleeble systems, Gleeble Application Note, DSI, Poestenkill NY, USA, 2001.

[3] Mandziej S.T.: Low-energy dislocations and ductility of ferritic steels, Materials Science & Engineering A, Vol. 164, 1993, p. 275.

[4] Kidin I.N.: Fizicheskie Osnovy Elektrotermicheskei Obrabotki Metallov i Splavov; Izd. Metallurgia, Moscow, 1969 (in Russian).

[5] Mandziej S.T., Výrostková A.: Accelerated Creep Testing of P91 weld metals, IIW Doc II-1461-02.